

2008

# Nondestructive detection and characterization of damages in honeycomb composite structures

Cory Foreman  
Iowa State University

Follow this and additional works at: <https://lib.dr.iastate.edu/rtd>

 Part of the [Mechanical Engineering Commons](#), and the [Structures and Materials Commons](#)

## Recommended Citation

Foreman, Cory, "Nondestructive detection and characterization of damages in honeycomb composite structures" (2008). *Retrospective Theses and Dissertations*. 224.  
<https://lib.dr.iastate.edu/rtd/224>

This Thesis is brought to you for free and open access by the Iowa State University Capstones, Theses and Dissertations at Iowa State University Digital Repository. It has been accepted for inclusion in Retrospective Theses and Dissertations by an authorized administrator of Iowa State University Digital Repository. For more information, please contact [digirep@iastate.edu](mailto:digirep@iastate.edu).

**Nondestructive detection and characterization of damages in honeycomb  
composite structures**

by

Cory Foreman

A thesis submitted to the graduate faculty  
in partial fulfillment of the requirements for the degree of  
MASTER OF SCIENCE

Major: Aerospace Engineering

Program of Study Committee:  
David K. Hsu, Major Professor  
Vinay Dayal  
Palaniappa A. Molian

Iowa State University

Ames, Iowa

2008

Copyright © Cory Foreman, 2008. All rights reserved.

## DEDICATION

I would like to dedicate this thesis firstly to my fiance, Meredith Ellis, for her patience and guidance through this process. Secondly to my parents, Tim and Kim Foreman, whom always believed in my potential, even in the hardest of times. And to my grandfather, Bill Nibbelink, who instilled in me a love for aviation at a very young age. Finally to my third grade teacher, Mrs. Overman. She provided me with hope at a time in my life when I needed it the most. I can most certainly say that this would not have been possible for me if these people had not been in my life.

## TABLE OF CONTENTS

<b>LIST OF TABLES</b> . . . . .	vi
<b>LIST OF FIGURES</b> . . . . .	vii
<b>ACKNOWLEDGEMENTS</b> . . . . .	xiii
<b>ABSTRACT</b> . . . . .	xiv
<b>CHAPTER 1. INTRODUCTION</b> . . . . .	1
<b>CHAPTER 2. COMPOSITE DEFECTS</b> . . . . .	3
2.1 DEFECTS IN THE LAMINATE . . . . .	4
2.1.1 DELAMINATION . . . . .	4
2.1.2 MICROCRACKING . . . . .	5
2.1.3 POROSITY . . . . .	6
2.2 DEFECTS IN THE CORE . . . . .	7
2.2.1 SKIN-TO-CORE DISBONDS . . . . .	7
2.2.2 CRACKING OR BUCKLING . . . . .	8
<b>CHAPTER 3. EXISTING INSPECTION METHODS</b> . . . . .	10
3.1 ULTRASONIC TRANSDUCTION . . . . .	10
3.1.1 DATA PRESENTATION . . . . .	14
3.1.2 FLAW DETECTION . . . . .	17
3.2 THERMOGRAPHY . . . . .	19
3.3 SHEAROGRAPHY . . . . .	22
3.4 LOW FREQUENCY TECHNIQUES . . . . .	23
3.4.1 TAP TEST . . . . .	23

3.4.2	MECHANICAL IMPEDANCE . . . . .	24
<b>CHAPTER 4. IMAGE PROCESSING . . . . .</b>		<b>26</b>
4.1	FOURIER TRANSFORMS . . . . .	26
4.1.1	MAGNITUDE VERSUS PHASE REPRESENTATION . . . . .	28
4.2	IMAGE ANALYSIS . . . . .	29
4.3	FILTERING . . . . .	32
4.4	PROGRAM . . . . .	34
<b>CHAPTER 5. COMPUTER AIDED TAP TEST . . . . .</b>		<b>40</b>
5.1	THEORY . . . . .	41
5.1.1	ACCELEROMETER SIGNAL OUTPUT . . . . .	42
5.1.2	EFFECTS OF DAMAGE . . . . .	43
5.1.3	EFFECTS OF IMPACT FORCE . . . . .	43
5.1.4	GRESZCZUK'S EQUATIONS . . . . .	44
5.1.5	GROUNDING SPRING MODEL . . . . .	45
5.2	APPLICATIONS . . . . .	47
<b>CHAPTER 6. HYSTERESIS . . . . .</b>		<b>50</b>
6.1	WHAT IS HYSTERESIS . . . . .	50
6.2	STATIC LOADING . . . . .	51
6.2.1	LOADING FRAMES . . . . .	51
6.2.2	TESTING FACTORS . . . . .	53
6.2.3	INITIAL TEST PANEL - CRACK VS BUCKLE . . . . .	56
6.2.4	SECOND TEST PANEL - IMPACT DAMAGES . . . . .	58
6.3	DYNAMIC LOADING . . . . .	62
6.3.1	DEDUCTION OF FORCE-DISPLACEMENT CURVES FROM ACCELERATION . . . . .	63
6.3.2	EXPERIMENTAL VERIFICATION . . . . .	69
6.3.3	STATIC VERSUS DYNAMIC LOADING . . . . .	72
6.3.4	STIFFNESS CORRELATION . . . . .	75

6.3.5 BELL TEST PANELS . . . . .	79
6.3.6 FUTURE WORK . . . . .	86
<b>CHAPTER 7. CONCLUSION . . . . .</b>	<b>88</b>
<b>BIBLIOGRAPHY . . . . .</b>	<b>90</b>

## LIST OF TABLES

Table 3.1	A comparison of the three different media used to transmit sound from the transducer to the structure . . . . .	11
Table 6.1	Properties of the test panel shown in Fig. 6.9 . . . . .	58
Table 6.3	Impact energies used to create damages on a thin-skinned honeycomb composite panel from Scaled Composites . . . . .	59
Table 6.2	Properties of the test panel shown in Fig. 6.11 . . . . .	59
Table 6.4	Properties of the test panel shown in Fig. 6.26 . . . . .	75
Table 6.5	Properties of the test panel shown in Fig. 6.30. Honeycomb cell size refers do the distance between two parallel walls . . . . .	81
Table 6.6	Impact energies of damages on Bell Helicopter panel A . . . . .	82
Table 6.7	Properties of the test panel shown in Fig. 6.31. Honeycomb cell size refers do the distance between two parallel walls . . . . .	82
Table 6.8	Impact energies of damages on Bell Helicopter panel B . . . . .	83
Table 6.9	Properties of the test panel shown in Fig. 6.32. Honeycomb cell size refers do the distance between two parallel walls . . . . .	83

## LIST OF FIGURES

Figure 2.1	Damage from an impact to the surface of the laminate forming delaminations and microcracking, porosity is a result of poor fabrication . . .	4
Figure 2.2	Microcracks shown forming as vertical lines in the matrix. Ply interfaces appear as horizontal lines in the micrograph . . . . .	5
Figure 2.3	Porosity shown forming in the matrix as well as in the resin-rich regions. Note the different types of morphology of the porosity in the different regions [2] . . . . .	6
Figure 2.4	Skin-to-core disbond resulting from an impact damage. The structure is composed of a fiberglass face sheet and a Divinycell foam core . . . .	7
Figure 2.5	Impact damage severe enough to cause damage to the laminate . . . .	8
Figure 2.6	Impact in a Nomex honeycomb core: Left-schematic of the damage. Right-sectioned structure back-lighted to show the fracture line in the honeycomb [3] . . . . .	8
Figure 2.7	Cracked Nomex core in a honeycomb composite sandwich caused by a static load of 750 lbs using a two inch diameter puck . . . . .	9
Figure 2.8	Buckled Nomex core in a honeycomb composite sandwich caused by a static load of 1000 lbs using a two inch diameter puck . . . . .	9
Figure 3.1	Path of the sound wave to the structure surface for three separate medium	10
Figure 3.2	Through-Transmission Ultrasonic (TTU) Testing . . . . .	12
Figure 3.3	Pulse-Echo Capture . . . . .	13
Figure 3.4	Pulse-Echo Capture showing a front surface echo, flaw reflection, and back surface echo . . . . .	13



Figure 3.5	Ultrasonic data presented in an A-scan format taken from [5] . . . . .	14
Figure 3.6	Ultrasonic data presented in an B-scan format . . . . .	16
Figure 3.7	Ultrasonic data presented in an C-scan format . . . . .	16
Figure 3.8	C-scan image using air coupled TTU . . . . .	18
Figure 3.9	The shadow effect a flaw has on the sound wave passing through the panel . . . . .	18
Figure 3.10	Effect of the double walls on an ultrasonic image in a honeycomb composite, the high intensity points tending to hide damaged regions . . .	19
Figure 3.11	Image of a metal to metal bonded aluminum honeycomb structure containing pocket damages produced using X-Ray(left) and optical shearography(right) obtained from [9]. The high intensity white region shown in the X-Ray image is an unknown damage . . . . .	22
Figure 4.1	Two dimensional Fourier Transform two images: Top-image containing a vertical pattern which show up in the FT as dots along the vertical axis, Bottom-same image only rotated 90 degrees, now the dots form on the horizontal axis in the resulting FT image . . . . .	30
Figure 4.2	Two dimensional Fourier Transform of an image in color . . . . .	31
Figure 4.3	Two dimensional Fourier Transform of a C-scan image of a honeycomb composite panel. Left: Spatial domain image, Right: Spatial Frequency domain image . . . . .	31
Figure 4.4	Initial filtering with high intensity points smoothed over . . . . .	32
Figure 4.5	Resulting inverse Fourier Transform of Fig. 4.4: Left-Original image, Right-Filtered image . . . . .	32
Figure 4.6	Filtered spatial frequency domain image using point smoothing, low-pass filter, and red reduction . . . . .	33
Figure 4.7	Resulting inverse Fourier Transform of Fig. 4.6: Left-Original image, Right-Filtered image . . . . .	34
Figure 4.8	2D FFT Image Cleaning Program: Console and Original Image . . . .	34

Figure 4.9	2D FFT Image Cleaning Program: Windowed Image . . . . .	35
Figure 4.10	2D FFT Image Cleaning Program: spatial Frequency domain Image . . . . .	36
Figure 4.11	2D FFT Image Cleaning Program: Point Filtering . . . . .	37
Figure 4.12	2D FFT Image Cleaning Program: Low Pass Filter . . . . .	38
Figure 4.13	2D FFT Image Cleaning Program: Inverse Fourier Transform . . . . .	39
Figure 5.1	Computer Aided Tap Testing System . . . . .	40
Figure 5.2	Honeycomb composite structure approximated as a grounded spring having a spring constant of $k$ . . . . .	41
Figure 5.3	Accelerometer signal output . . . . .	42
Figure 5.4	Effect of a flaw on the accelerometer signal . . . . .	43
Figure 5.5	Accelerometer signal output at an undamaged region(left) and a damaged region(right), representing soft, medium, and hard tap forces for each case. The impact duration(contact time) of all three curves was about $250\mu s$ for the undamaged and $500\mu s$ for the damaged region . . . . .	44
Figure 5.6	Experimental data showing the agreement between stiffness deduced from tap test data and stiffness directly measured in static loading tests . . . . .	47
Figure 5.7	Tap test image of a B767 outboard spoiler, test performed on the flat side of the spoiler . . . . .	48
Figure 5.8	Tap test image of a C-5 Torque Deck . . . . .	48
Figure 6.1	Typical stress-strain curve showing a hysteresis effect . . . . .	50
Figure 6.2	Imada loading frame mounted with an Imada force gauge(bottom right) and displacement dial gauge(top right) . . . . .	52
Figure 6.3	Sample bay on the INSTRON testing machine . . . . .	53
Figure 6.4	INSTRON testing machine . . . . .	53
Figure 6.5	Effect of the step size variation on the hysteresis loops during static loading . . . . .	54
Figure 6.6	Impact of step size variation on the loop areas during static loading . . . . .	55

Figure 6.7	Effects of relaxation in the structure on the measured load . . . . .	56
Figure 6.8	Test panel cut into strips so that the damage to the honeycomb could be examined . . . . .	56
Figure 6.9	Two test strips used for experiments: Panel C1-8(left) containing a crack in the honeycomb core, panel C2-7(right) containing a buckle in the honeycomb core . . . . .	57
Figure 6.10	Hysteresis loops taken on panels C1 and C2 as well as an undamaged panel . . . . .	58
Figure 6.11	Test panel from Scaled Composites . . . . .	58
Figure 6.12	Hysteresis loops produced from the Scaled Composites test structure when statically loaded using the manual loading setup . . . . .	60
Figure 6.13	Energy absorbed by the Scaled Composites test panel derived from the corresponding hysteresis loops . . . . .	61
Figure 6.14	Absorbed energy curve on Scaled Composites panel using INSTRON machine . . . . .	61
Figure 6.15	Typical acceleration curve produced from a tap . . . . .	63
Figure 6.16	Area under the curve between two adjacent points using discrete data	64
Figure 6.17	Theoretical acceleration, velocity and displacement curves as well as a hysteresis loop calculated from an acceleration curve approximated by a bell curve. For simplicity the displacement was plotted as the negative of its calculated value . . . . .	67
Figure 6.18	Theoretical acceleration, velocity and displacement curves as well as a hysteresis loop calculated from an asymmetric acceleration curve. For simplicity the displacement was plotted as the negative of its calculated value . . . . .	68
Figure 6.19	Experimental setup used to measure total displacement of an accelerom- eter attached to a cantilever beam . . . . .	69
Figure 6.20	Cantilever beam being held by the electromagnet . . . . .	70

Figure 6.21	(Top) Voltage output from the accelerometer, (Middle) Velocity integrated from acceleration with $V_0 = 0$ , (Bottom) Displacement integrated from velocity with an initial condition of $D_0$ . . . . .	71
Figure 6.22	Correlation between calculated distance using the accelerometer output and the measured distance . . . . .	72
Figure 6.23	Hysteresis loops taken on the Scaled Composites panel using dynamic loading . . . . .	73
Figure 6.24	Comparison between static and dynamic loading: (Left) loops taken over an impact damage of 4.04J on the Scaled Composites panel, (Right) loops taken over an impact damage of 4.71J on the Scaled Composites panel . . . . .	74
Figure 6.25	Comparison between static and dynamic loading where both load and displacement have been normalized to one: (Left) loops taken over an impact damage of 4.04J on the Scaled Composites panel, (Right) loops taken over an impact damage of 4.71J on the Scaled Composites panel . . . . .	74
Figure 6.26	Test panel used for stiffness correlation . . . . .	75
Figure 6.27	Expected accelerometer output versus actual accelerometer output showing the drop below the baseline . . . . .	77
Figure 6.28	Effect of the gripping force on the accelerometer when used in a hand tap. Time Scale: 0.1ms per division, Voltage Scale: 1.00V per division . . . . .	78
Figure 6.29	Correlation between the stiffness computed from tau and the stiffness computed from the force-displacement curve. The data points were collected over a 17x25 grid (425 data points) . . . . .	79
Figure 6.30	Bell Helicopter test panel A . . . . .	81
Figure 6.31	Bell Helicopter test panel B . . . . .	82
Figure 6.32	Bell Helicopter test panel C . . . . .	83
Figure 6.33	Contour images taken from Bell Helicopter panel A . . . . .	84
Figure 6.34	Contour images taken from Bell Helicopter panel B . . . . .	85

Figure 6.35 Contour images taken from Bell Helicopter panel C . . . . . 86

## ACKNOWLEDGEMENTS

I would like to take a moment to express my gratitude to those that provided me with assistance during the completion of the thesis. First and foremost, Dr. Dave Hsu and Dan Barnard for providing expert advice when needed and supporting me through the research and writing of this thesis. I would also like to thank my committee members for their efforts and contributions to this work: Dr. Vinay Dayal and Dr. Palaniappa A. Molian. Dr. John Basart provided much help on the two dimensional Fourier transforms used in the image processing routines. Finally I would like to thank Jeff Neissen from Bell Helicopter for providing industrial grade samples which were used extensively during this research.

## ABSTRACT

This thesis discusses many existing methods of nondestructive evaluation used on honeycomb structures ranging from ultrasonic transduction to various low frequency techniques. The focus, however, is given to a newly developed technique based on hysteresis effects in force-displacement curves. The area enclosed by the hysteresis loop represents the amount of energy absorbed by the sample during the loading and unloading phases. It is believed that the cause of the energy absorption is due to increased internal frictional losses which occur when the sample is damaged. The loop area was found to correlate well with the level of damage sustained by the structure. This technique is centered on the deduction of a force-displacement curve from an accelerometer tap, which allows the force-displacement curves to be generated from a single tap on one surface of the structure.

Traditionally a force-displacement curve, the equivalent of a stress-strain curve, is produced using a mechanical testing machine. However, this is not a suitable method to be used to attain a force-displacement curve while a structure is in-service because it requires access to both the front and back surfaces of the structure. The deduction of a force-displacement curve from an accelerometer tap proved to be an effective solution to this problem. The great advantage of this method is that it only requires access to one surface of the structure to generate a force-displacement curve. This method also takes much less time to generate the hysteresis loops. A mechanical testing machine could take up to 15 minutes to produce a single force-displacement curve, this method will produce the same curve in seconds. Much of this research was devoted to the testing and development of the techniques used to deduce a force-displacement curve from an accelerometer tap.

This thesis also takes a look at the benefits of two-dimensional Fourier Transforms. During

the course of this research, many C-scans of honeycomb composite structures were generated using air-couple ultrasonics. These C-scans were used as baseline images to compare with the results of the newly developed mechanical hysteresis technique. The honeycomb structure can cause very distracting hexagonal patterns in ultrasonic images. The Fourier transform and the processing associated with it is able to suppress these distracting patterns while leaving the rest of the image relatively unaffected. In some cases, not only can the patterns be suppressed, but the flaws can also be drawn out. A program was written to perform and filter the two-dimensional Fourier Transforms to suppress the patterns from the C-scan images.



## CHAPTER 1. INTRODUCTION

On the eighth of July, 2007, The Boeing Company, a major airline manufacturer, unveiled its first 787 Dreamliner at a roll out ceremony in Everett, Washington. This unveiling was highly anticipated due to the materials used to construct this aircraft. Fifty percent of the 787 is made of composite materials, most of which come in the form of carbon fiber reinforced plastic. Nearly the entire fuselage is made of composite material in the form of composite barrels, each of which is manufactured in one piece. This eliminates the need for many rivets commonly seen on existing airlines. Using such an immense amount of composite material was previously unheard of for a major airline; the Boeing 777 only contains 15 percent composite material, with the majority of the aircraft being composed of aluminum.

The 787 takes advantage of composite's superior strength-to-weight ratio compared to most metals. Boeing boasts about much higher fuel efficiency, claiming to be at least 20 percent more efficient than the current competing airliners. Boeing also states that the 787 will fly much faster than existing airliners, achieving cruise altitude speeds of up to Mach 0.85. Nevertheless, even with the great benefits composites have to offer, Boeing still faced much resistance for using this revolutionary material.

The Dreamliner also makes use of honeycomb composites in locations such as the leading edge of the wing, control surfaces, and the interior of the aircraft. A honeycomb composite differs from a solid laminate in its structure. If a solid laminate were a solid plate, then a honeycomb composite would be an I-beam. The honeycomb composite makes use of a light weight material, such as Nomex, fashioned into a honeycomb structure with a high load bearing ability in relation to its weight. The honeycomb is then sandwiched between two face sheets which are solid laminates. The I-beam structure the honeycomb takes on gives it a much

higher critical bending load than a solid laminate while keeping the light weight advantages of composites.

Aluminum has a long history with aircraft, having a well-defined set of inspection techniques able to be used in the field. Being a relatively new material, composites do not have this luxury; composites, unlike aluminum, can have defects embedded within the material, ranging from delaminations between plies to microcracks and porosity in the matrix. Most cracks in aluminum propagate to the surface because they do not have to cross material interfaces, making them easily detectable. Cracks in composites however are stopped by each ply interface, making them much more difficult to detect. As a result, structural uncertainties require airplane manufactures to over design composite aircraft, taking away much of the light weight advantages of the composite material.

Nondestructive evaluation gives manufacturers the ability to reduce or eliminate the over design of composite materials, allowing them to make full use of their lightweight advantage. The name given to this evaluation method is self-explanatory, composites can be inspected without destructively affecting the material to determine if there is any hidden damage. However, when these materials are designed this way, nondestructive evaluation finds importance in the factory as well as on the hanger floor. The structures must then be routinely inspected to ensure that damage has not been induced while the structure is in-service. For this reason the development of nondestructive techniques is essential to the use of composites within any structure.

A focus on honeycomb composites and their associated damages must be outlined in order to evaluate the new detection techniques developed throughout the course of this research. Various different detection techniques have been addressed, ranging from the tap test to air coupled ultrasonics. The new technique, hysteresis, relies on the deduction of a force-displacement curve from acceleration and comes closely related to the tap test. Although it is performed in the same manner, more information can be collected in the same process, revealing more about the material.

## CHAPTER 2. COMPOSITE DEFECTS

Unlike their aluminum predecessors, composite materials are usually immune to many of the forms of deterioration that plagued aluminum and most other alloys. Cracking and corrosion were costly and limited the service life of these materials on aircraft structures [1]. Yet, in spite of such a high strength-to-weight ratio, composite materials often tend to be easily damaged in their service life; simple common occurrences, such as an impact from a dropped tool, can cause a host of hidden damages within the composite structure.

Composite materials have a variety of damage types. Three basic forms of defects exist: delaminations, microcracking, and porosity, all of which commonly occur in the solid laminate face sheets. Causes can range from poor layup conditions to damages on the material while in service. When considering sandwiched composites, damages within the core also emerge. In the core, failure can take the form of cracks or buckles when the structure is exposed to excessive loads. In addition, the bond between the face sheet and the core becomes susceptible to damage, causing a skin-to-core disbond. Typically in sandwich composites, damages in the core occur before damages in the face sheet.

When a composite part is damaged, it usually contains several varieties of flaws. Impact damaged regions will contain delaminations, microcracking, fiber breakage, skin-to-core disbands, and core cracking or buckling. Any assortment of cracking can allow corrosive fluid to leak into the core of the sandwiched panel. Hydraulic fluid can deteriorate the adhesive adjoining the laminate and the core, which would then lead to further damage to the structure. The result resembles a cascading effect, in which one flaw will lead to another when allotted enough time. This fact only reinforces the need to be able to quickly characterize and repair these flaws in a nondestructive manner.

## 2.1 DEFECTS IN THE LAMINATE

In a composite structure, the laminate constitutes a composition of materials made up of fibers and resin matrix. Several plies are built up to form the face sheet or laminate. In sandwiched composites, the face sheet is attached to the top and bottom surfaces of the core sandwiched panel. The face sheet tends to be more resilient to damage than the core, though damage can still occur. Many times the damages can occur before the structure has ever entered service. Poor layup conditions or flawed fabrication can cause various types of defects in the face sheet. The majority of in-service damages in face sheets come from impact damages, which can cause various defects within the layup, some of which remain hidden to the naked eye.

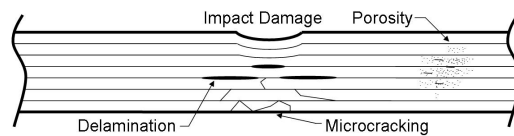


Figure 2.1 Damage from an impact to the surface of the laminate forming delaminations and microcracking, porosity is a result of poor fabrication

### 2.1.1 DELAMINATION

A delamination occurs when a gap forms between two plies of different fiber orientation. Due to the fact that these composites are usually assembled ply by ply, poor layup conditions can be a cause of delaminations. If manufacturing conditions are not clean, unwanted particles, such as dust, can be introduced into the interface between the plies. Faulty bonding conditions will result, which leads to a delamination.

There exists a resin rich area which will be lacking in fibers. This area, shown in Fig. 2.3, will often occur between two separate plies. This section is the weakest point of the two ply region and as a result becomes a failure point when the structure is put under a load. When subjected to an excessive load, this area can become starting point for a delamination between the two plies to form.

The orientation of these delaminations is unique when they are formed through an impact damage. The delaminations come in pairs and are usually symmetric about the center of the impact. If the delaminations are inspected ply-by-ply, their direction will change with the orientation of the fibers. If the panel is a 0-90 layup, the pattern formed by the delaminations is similar to the shape of a dumbbell. With more fiber orientations introduced, the number of lobes will increase, forming a new pattern.

### 2.1.2 MICROCRACKING

In addition to delaminations, matrix microcracking also presents itself as a common defect in solid laminates. It is one of the many types of defects associated with impact damages, yet the damage can be caused by thermal cycling as well. Fig. 2.2 shows a micrograph of a composite laminate having carbon cyanate ester composition. This structure was thermally cycled from room temperature to cryogenic temperatures several times to induce severe matrix microcracking.

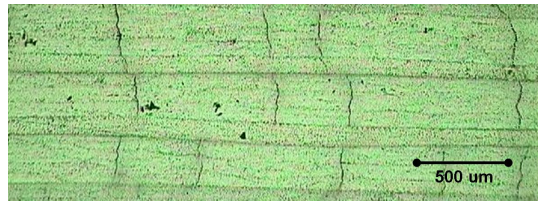


Figure 2.2 Microcracks shown forming as vertical lines in the matrix. Ply interfaces appear as horizontal lines in the micrograph

The microcracks will propagate until they encounter an interface having a different fiber orientation; the cracks will soon after change direction or stop. In Fig. 2.2, the microcracks are the vertical lines that show up between plies. These microcracks will reduce the strength of the composite and can also cause a path for corrosive fluid to infiltrate the sandwiched panel and cause more damage. For this reason, microcracks can also be very difficult to detect. When using surface couplants such as water, gel, or oil during ultrasonic nondestructive evaluation; the couplant itself will seep in and fill these cracks. This will make the microcracks invisible on the ultrasonic image and therefore undetectable. If the microcracks are free of any fluid, a

heavily microcracked region will show up as a region of excessive attenuation on an ultrasonic image.

### 2.1.3 POROSITY

Porosity occurs exclusively during fabrication of the laminate and many techniques are utilized during layup specifically designed to suppress porosity. Like microcracking, porosity only occurs in the matrix, leaving the fibers relatively unaffected. Fig. 2.3 exemplifies how heavily porosity content can affect a structure. The porosity shown in this figure tends to form in two different regions, the resin-rich areas as well as in between the fibers; each area has a different type of morphology associated with it. Porosity occurs because of volatile gas released from the resin during curing. If the gas is unable to escape, it forms pockets within the matrix which will harden after the structure has finished curing. Vacuum bags are always used during manufacturing to pull a vacuum on the structure in order to draw out these gases.

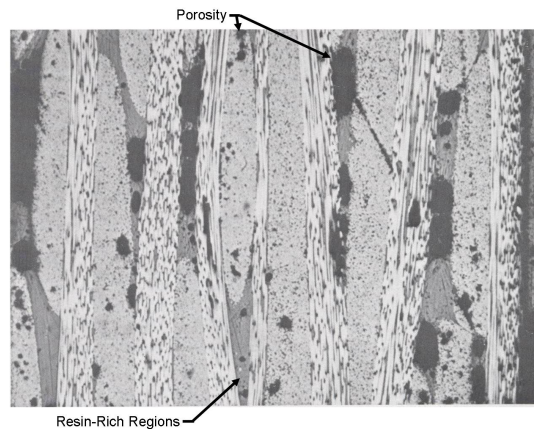


Figure 2.3 Porosity shown forming in the matrix as well as in the resin-rich regions. Note the different types of morphology of the porosity in the different regions [2]

Porosity does not affect the structure as heavily as microcracking or delaminations, so a certain level of it can be tolerated. Complete elimination of porosity proves to be challenging; vacuum bags can be very difficult to attach to complex shapes while retaining the ability to hold a tight vacuum during the entire curing process. For this reason, over design is occasionally

needed when fighting porosity.

## 2.2 DEFECTS IN THE CORE

The core of a sandwiched composite material is more easily damaged than the face sheet. Impact damages will usually have the most effect on the core of the composite, causing cracking, buckling, and skin-to-core disbonds. Extreme damages will also show up in the face sheet. In addition, corrosive fluids which leak into the core of the composite can also lead to damages. These fluids will deteriorate the adhesive bonds between the core and the face sheets, causing skin-to-core disbonds. These disbonds can cause failure of the structure when subjected to a cyclical load.

### 2.2.1 SKIN-TO-CORE DISBONDS



Figure 2.4 Skin-to-core disbond resulting from an impact damage. The structure is composed of a fiberglass face sheet and a Divinycell foam core

Skin-to-core disbonds occur in the region between the face sheet and the core of the composite. Fig. 2.4 shows a sandwiched composite containing a foam core. Although it is not honeycomb, the two possess surprising similarities in their damage morphology. The top portion of the image reveals the face sheet, made up of a fiberglass/epoxy layup, while the bottom shows the Divinycell foam core. The illustrated structure has a severe impact damage to its surface and a resulting skin-to-core disbond. The reason for the gap between the face sheet and the core is due to the elasticity of the face sheet. After an impact damage, the face sheet

has a tendency to spring back to its original shape; although, if the damage is severe enough, it will retain some deformation as shown in Fig. 2.5. The core is very brittle and does not have the capability to return to its original shape. The adhesive layer is broken and the core and the face sheet become separated.



Figure 2.5 Impact damage severe enough to cause damage to the laminate

The adhesive layer can also be degraded chemically. If liquids such as hydraulic fluid are allowed to seep into the composite core, break down of the adhesive bond can occur. Although there is usually no damage to the core or the face sheet, simply weakening the adhesive layer can cause failure.

### 2.2.2 CRACKING OR BUCKLING

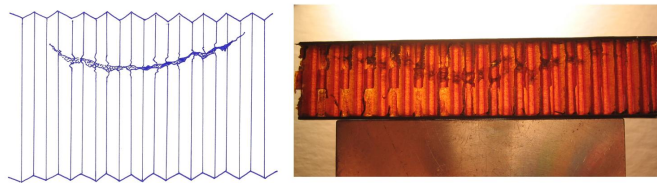


Figure 2.6 Impact in a Nomex honeycomb core: Left-schematic of the damage. Right-sectioned structure back-lighted to show the fracture line in the honeycomb [3]

Cracking or buckling takes place when a sandwiched composite is put under an excessive compressive load. When the load exceeds the limit of the structure, the core buckles and leaves a fracture line in the core which often takes the shape of a “smile” centered below the impact site. The crack or buckle can even reach depths of up to one half the thickness of the



sandwiched structure [3]. Fig. 2.6 illustrates the effect of an impact damage on a honeycomb core. The sectioned structure is back-lighted to make the fracture more visible.

Cracking or buckling of the core will severely reduce the stiffness of the composite. Fig. 2.7 and Fig. 2.8 show the difference between a crack and a buckle. Both the crack and the buckle will take the same shape, which appear to be common among any type of core material. As shown in the previous section, this type of morphology was also observed in foam cored composites.



Figure 2.7 Cracked Nomex core in a honeycomb composite sandwich caused by a static load of 750 lbs using a two inch diameter puck

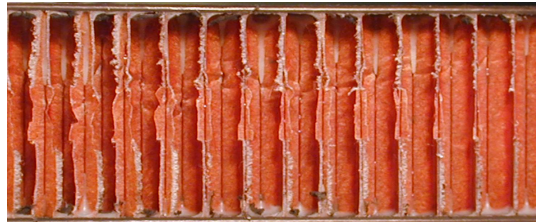


Figure 2.8 Buckled Nomex core in a honeycomb composite sandwich caused by a static load of 1000 lbs using a two inch diameter puck

The level of damage to the core cannot always be determined by visual inspection. Between Fig. 2.7 and Fig. 2.8, the cracked panel, Fig. 2.7, appears to be more heavily damaged. Yet, the buckled panel, Fig. 2.8, was loaded to a higher load before failure. Cracks typically appear to have more damage associated with them upon visual inspection; however, experimental results show that this observation is not always the case. It is unknown why the core would crack versus buckle; this would obviously be dependent upon the properties of the honeycomb. In this case, both panels contained identical honeycomb material.

## CHAPTER 3. EXISTING INSPECTION METHODS

### 3.1 ULTRASONIC TRANSDUCTION

Ultrasonic transduction is a very popular technique used to inspect composite structures. It is able to detect delaminations, microcracking, porosity, skin-to-core disbonds, and a host of other defects common among composite materials. Ultrasonic transduction can also inspect relatively thick materials by using a range of frequencies. A selected frequency is dependent upon the medium used and the thickness of the material, where lower frequencies are able to penetrate further into the material. Lower frequency, however, comes at an expense of lower resolution of flaws in the resulting image. Ultrasonic transduction is also hampered by very expensive and complex scanning systems needed to collect the data and generate an image.

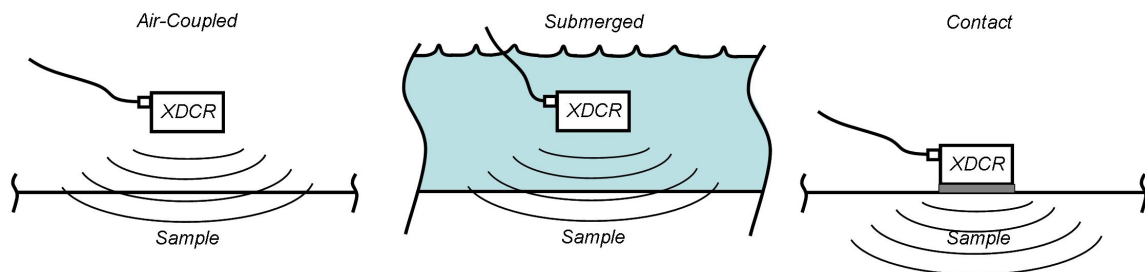


Figure 3.1 Path of the sound wave to the structure surface for three separate medium

With the use of ultrasonic transduction three common medium are used to propagate the sound to the structure surfaces: water, gel or oil, and air. Each medium affects the sound differently and has advantages and disadvantages among the other substances. The properties

Method	Medium	Sound Velocity $\left(\frac{mm}{\mu s}\right)$	Acoustic Impedance $\left(\frac{Kg}{s \cdot m^2}\right)$	Frequency Range (MHz)
Submerged	Water	1.497	1 480 000	1 to 50
Contact	Gel or Oil	1.477	1 190 000	1 to 50
Air-Coupled	Air	0.344	415	0.05 to 0.5

Table 3.1 A comparison of the three different media used to transmit sound from the transducer to the structure

of the three media are outlined in Table 3.1 and an illustration of the process is shown in Fig. 3.1. Currently, water is the most convenient medium. The structures to be inspected are either submerged in a pool of water large enough to accommodate the structure or advanced scanning systems spray a jet of water onto the surface of the structure. The sound follows the jet of water to the structure surface and back to the receiver. Exposing some composite materials to water can lead to damage, posing a disadvantage for this assessment method. Some sandwiched composites cannot be inspected using a water medium because they are not water tight. Water leakage into the honeycomb cells causes internal damage to the honeycomb structure. Thus, air coupled scanning systems are becoming of interest.

Air coupled ultrasonic scanning is a non-intrusive procedure; there are no liquids or gels making contact with the structure surface. The absence of liquids is a great advantage because it simplifies the process; ultimately increasing its speed and efficiency. Nevertheless, air coupled scanning is still not widely used in industry. Using air as a medium to pass sound through requires much lower frequencies because air has a much higher attenuation in comparison to other common medium. Low transmission coefficients, which will be discussed later in this paper, also plague this method. Not only does this reduce the resolution of the image, but it also requires air coupled scanning to be strictly a two sided method. A two sided method requires access to both the front and back surface of the panel. A full understanding of this result requires the analysis of different types of techniques used to capture the sound wave after it has passed through the panel.

The simplest way to capture sound is to place a receiving transducer on the opposite side of the panel. This process, called through-transmission ultrasound(TTU), can be achieved using

any medium. The TTU method, as aforementioned, requires access to both the front and back surface of the panel, which may not be a problem in a factory setting, but in-service composite materials also require in-service inspection, where access to the back surfaces is many times unattainable.

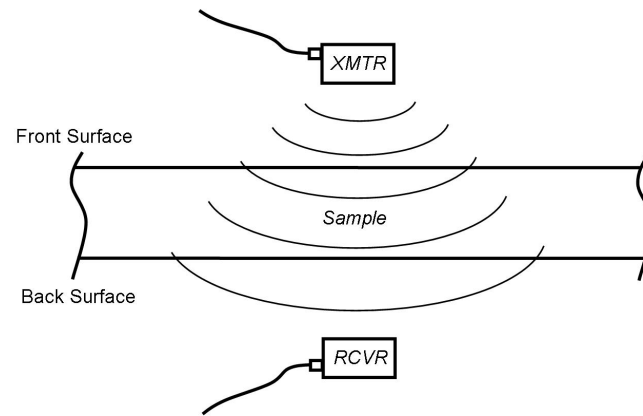


Figure 3.2 Through-Transmission Ultrasonic (TTU) Testing

Another technique called pulse-echo capture only requires access to one side of the structure. This method works by making use of the back surface reflected wave. Each time an acoustic wave encounters an interface of two different media, part of it is transmitted through the interface and the remainder becomes reflected. If the wave is at a normal incidence angle to the interface, the sound is reflected directly back on the same path; hence, the transmitter will then also act as a receiver. The depth of the flaws can also be determined by using the flaw itself as a “mirror” to reflect the sound back to the receiver. Although, to make use of this technique, time of flight data must also be recorded (where time of flight is simply the amount of time it takes the sound to travel from the face of the transducer to the structure surface and back again). This method, however, cannot penetrate thick materials like the TTU method can simply because it must travel through the entire thickness twice, in effect doubling the attenuation caused by the panel. This method is far superior to TTU in the fact that it only requires one transducer and access to only one side of the panel. It is able to acquire more information about the flaw; nonetheless, this is all contingent upon the ability to get a clear

signal back to the transducer.

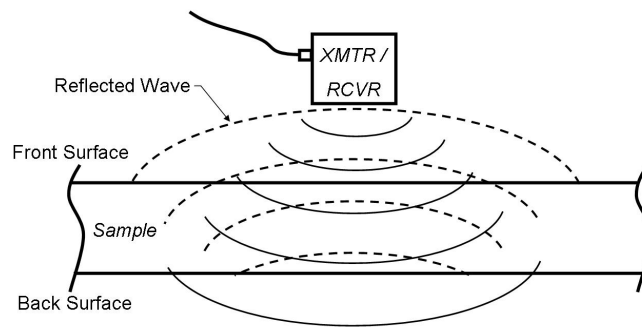


Figure 3.3 Pulse-Echo Capture

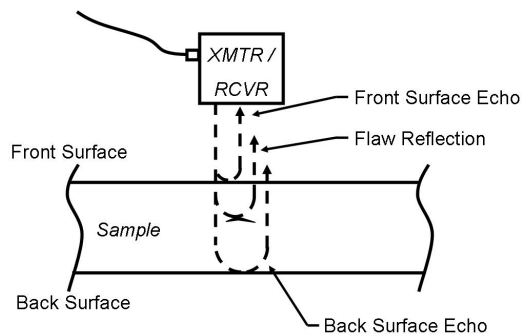


Figure 3.4 Pulse-Echo Capture showing a front surface echo, flaw reflection, and back surface echo

The impedance mismatch of air to any solid [4] is generally what prevents air-coupled scanning from making use of the pulse-echo capture technique. The acoustic impedance of air is much lower than that of most solid materials, shown in Table 3.1, which results in very high reflection coefficients at the air-solid and solid-air interfaces. Guiding sound to the structure surface is relatively easy when using air as a medium; however, propagating that sound wave into the structure proves to be very challenging. For example, when a sound wave intersects the structure surface while using air as a medium, an acoustic wave penetrates into the material

which has much less than one percent of the magnitude of the original acoustic wave. As a result, a very long tone burst, usually around  $80 \mu s$ , is needed to provide enough energy to pass through two interfaces and still retain a clear signal to be received. The tone burst is too long to distinguish between front and back surface echoes; hence, the method cannot be used because the signals are overlapping (causing constructive and destructive interference). An illustration of the TTU and Pulse-Echo can be seen in Fig. 3.2 and Fig. 3.3 respectively. Fig. 3.4 shows the various reflections captured when using a pulse-echo method.

Although air coupled transduction cannot make use of the pulse-echo technique, the TTU method it does make use of can also provide much information about the structure. Impact damages and disbonds are easily detected and usually clearly appear on the resulting image. An example of a C-scan image produced with air coupled TTU is shown in Fig. 3.8.

### 3.1.1 DATA PRESENTATION

When using an ultrasonic scanning system, there are three common methods to present the data; they are traditionally designated A-scan, B-scan, and C-scan. Each method is very different and can express varying aspects about the detected flaws. The A-scan is a very

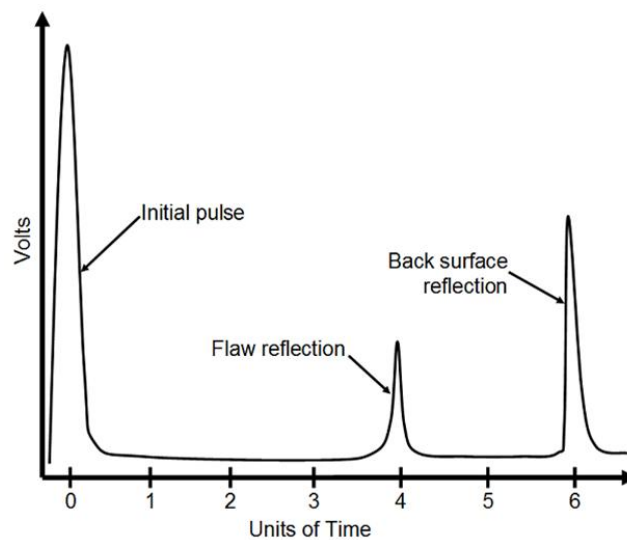


Figure 3.5 Ultrasonic data presented in an A-scan format taken from [5]

basic way to present ultrasonic data. Fig. 3.5 shows an A-scan trace where the data is plotted

as the signal amplitude versus time. An A-scan only gives information corresponding to one location on the structure. The depth of the flaws and the panel thickness can be determined if the velocity of sound is known for the given material. Oscilloscopes are the most commonplace A-scans are utilized; they are the standard form of data presentation for an oscilloscope. Although very useful, the A-scan cannot give much information about the entire structure unless combined with a C-scan. This particular A-scan, shown in Fig. 3.5, is making use of a pulse-echo capturing technique with the transducer in contact with the surface of the structure. For this reason there is no front surface echo because it is absorbed in the initial pulse; however, the flaw reflection and the back surface echo are still visible. These features are also shown in Fig. 3.4.

Several A-scans are combined together to form a B-scan. The traditional B-scan is a unidirectional scan plotting the time versus position. An A-scan is taken for every position along a line, they are then stacked next to each other. A gray or color scale is now used to represent the amplitude of each A-scan along a line. Most of the A-scan is a flat line very near zero; however, when a reflection is encountered the amplitude will begin to change swinging both positive and negative. These reflections will show up in the B-scan as lines of a different color. The front and back walls of the panel and flaws contained within the panel will cause a reflections and will be apparent in the B-scan. Fig. 3.6 shows an example of a B-scan graph where front surface, back surface, and flaw reflections are shown. A B-scan can very clearly show relative information about the depth of the flaws contained within the sample.

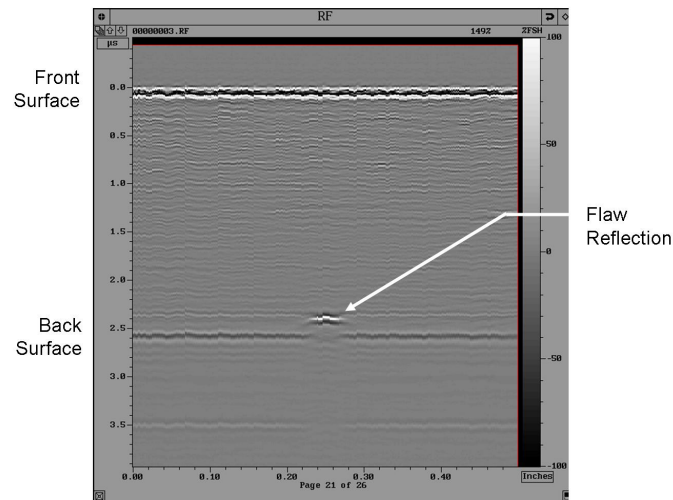


Figure 3.6 Ultrasonic data presented in an B-scan format

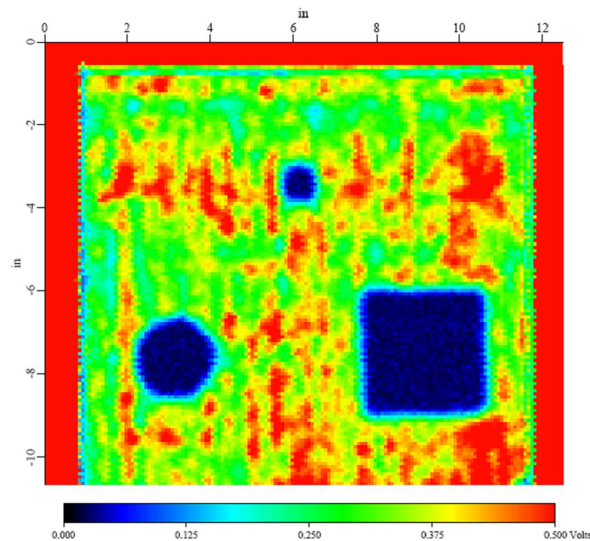


Figure 3.7 Ultrasonic data presented in an C-scan format

The final data presentation mode is the C-scan. The C-scan requires measurement of three parameters: x position, y position, and signal amplitude. The C-scan will make a 2D raster contour plot to represent the signal amplitude at a specified position in the A-scan at each point over the surface of the panel. A gating system can be created where each point in the



C-scan represents the maximum value of the A-scan within the gate. The width of the gate represents a portion of the thickness of the panel, where lower values of time-of-flight are closer to the surface. A C-scan can be looked at as a flat horizontal cut of the panel, where only a slice of the thickness is being inspected. If a flaw is present, the signal will either be blocked when using TTU, or shifted when using pulse-echo. Flaws are then usually represented as low amplitude(TTU) or high amplitude(pulse-echo) regions in the resulting image. Fig. 3.7 shows a TTU C-scan of a honeycomb composite with three embedded flaws. The flaws are clearly visible in the C-scan image as dark blue regions.

C-scans are presently the most common types of data presentation because they are the most informative for analyzing an entire structure; however, when using newer systems with the ability of full-waveform capture, all three types of data presentation can be captured at once. This allows B-scans to be two dimensional and C-scans to be obtained for the entire depth of the panel. The ability certainly gives a great deal of information about the structure; however, it requires powerful computers and a great deal of memory to store the data for large scans. Visual flaw detection methods will almost always use a B-scan or C-scan image to detect the flaws. It should be noted that an A-scan is usually needed to set up the gates needed for both the B-scans and C-scans. Although the final results are usually shown as B-scans or C-scans, the A-scan was very likely utilized at one point during the data collection process.

### 3.1.2 FLAW DETECTION

When an acoustic wave encounters a flaw in a panel such as a void, nearly the entire sound wave is reflected back toward the transducer, in effect, casting a shadow over the flawed region. This is illustrated in Fig. 3.9. These shadows show up as abnormalities in the resulting C-scan image. In Fig. 3.8, these abnormalities are the blue spots on the image which can be easily seen with the naked eye. However, the severity of the flaw remains unknown. Many times every flaw will show up as a dark region with lighter edges, caused by the sound wave only being partially blocked by the flaw at its edges due to diffraction and the sound wave scattering around the flaw. Every flaw will show up as the same color within the image, only varying in

size and not in severity.

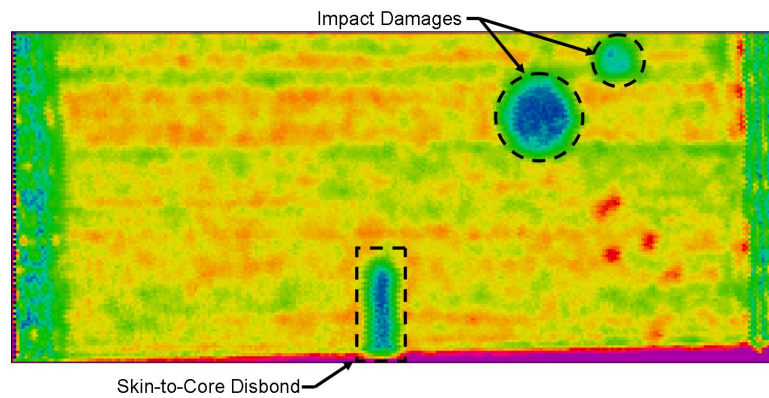


Figure 3.8 C-scan image using air coupled TTU

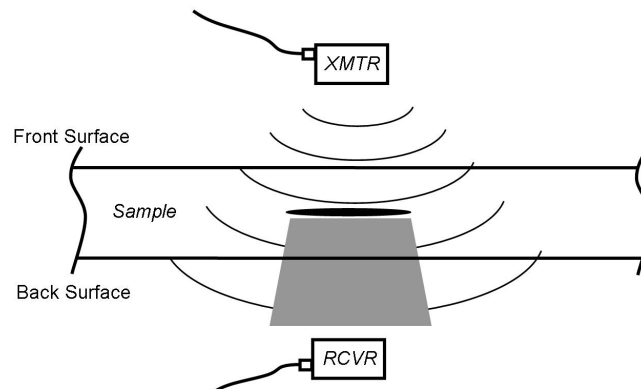


Figure 3.9 The shadow effect a flaw has on the sound wave passing through the panel

There are drawbacks to ultrasonic transduction in honeycomb composites. When a sound wave passes through a honeycomb composite, the double walls in the honeycomb cell provide much stronger transmission coefficients than the other cell walls or the air gap. This causes bright dots to show up in the image. They are distracting and can conceal damaged areas from the naked eye. Fig. 3.10 demonstrates this double wall effect on an TTU image, showing how distracting the periodic pattern can be in regards to detecting damaged areas. Image

processing techniques can be used to reduce these distractions.

Image processing techniques can be used to bring out the flaws in these images so that they may be more easily detected by the human eye. During the course of this research, a method using two dimensional Fourier Transforms was developed specifically for honeycomb composite structures to be used on images like the one shown in Fig. 3.10. The periodic pattern of the double walls can be advantageous. A two dimensional Fourier Transform can be used to nearly completely remove these patterns from the image and will be outline in detail in Chapter 4.

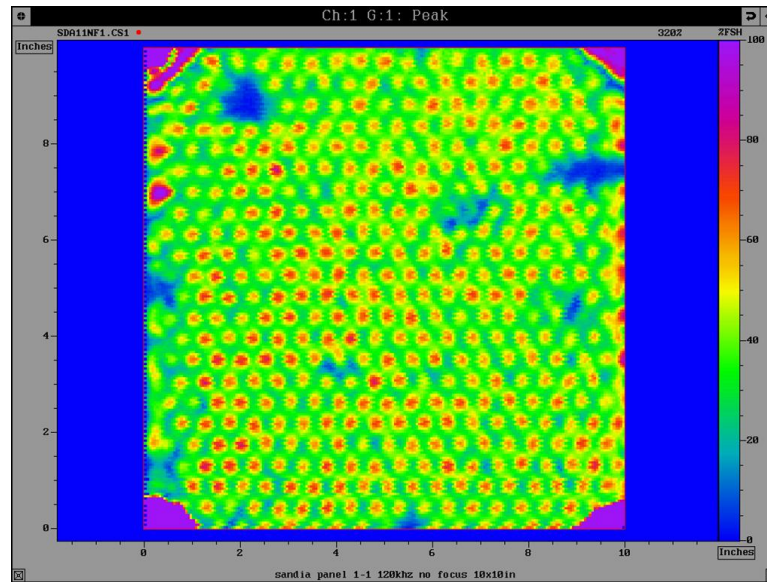


Figure 3.10 Effect of the double walls on an ultrasonic image in a honeycomb composite, the high intensity points tending to hide damaged regions

### 3.2 THERMOGRAPHY

While ultrasonics makes use of sound waves propagating through a material, thermography makes use of thermal waves propagating from the surface into the material. These waves are outside the visible spectrum of light, having longer wavelengths than those contained within the visible spectrum of light. This section will outline three types of methods involving infrared thermography which are actively being used as nondestructive techniques; they include:

Traditional Thermography, Flash Thermography or Thermal-Wave Imaging, and VibroThermography.

Infrared thermography makes use of the thermal conductivity of the inspected materials. It has been shown that when a material contains voids or pores within its structure, the thermal properties of that material are affected [6]. For example, a delamination is a material discontinuity across which no thermal waves can propagate. As a structure is inspected, the differences in the thermal properties of damaged regions versus non-damaged regions will be apparent in the image produced by an infrared camera.

Traditional thermography deals with the slow heating and cooling of the structure. Many times heat lamps are used to heat the structures while an infrared camera inspects the surface of the structure. Differences in the thermal properties in the structures will be revealed in the IR image. However, the structures do not always need an external heating source to be inspected. If a structure experiences a thermal change from its in-service conditions to its out-of-service conditions, infrared cameras can be used after the structure has returned from service. The inspection simply takes place as the structure begins to return to its ambient temperature.

The second method is much like traditional thermography; however it takes place on a much different time scale. Flash Thermography uses an external heating source to heat up the structure surface with a quick burst of energy, after which the surface temperature will be monitored with an infrared camera as a function of time. As the structure cools, the thermal differences within the structure will become apparent on the resulting image as they will disrupt the heat flow through the structure.

Flash thermography can also be referred to as Thermal-Wave Imaging. These methods monitor how the thermal waves move through the structure. These thermal waves propagate from the heated region and interact with the surrounding material. If the region has different thermal properties than its surroundings, it will cause the thermal waves to reflect and scatter in a manner much alike conventional wave propagation theory. Resulting images of the structure are obtained from the scattered or reflected thermal waves. These methods by which these

waves are captured can become very complicated and are not the subject of this section. Further information about the capturing techniques is discussed in the referenced material [8]. The drawback to this techniques is that it only has the ability to detect flaws very near the surface of the structure. The thermal waves are only able to travel one to two wavelengths before their amplitude becomes negligibly small [8]. Nevertheless, subsurface defects such as voids, delaminations, and cracks are readily detectable using this method.

The final method of inspection is VibroThermography. First discovered in the 1970 when it was observed that as a panel containing cracks or discontinuities was being excited with high energy, low frequency ultrasound, the defects would generate heat and become detectable using an infrared camera[7]. The method is performed by placing an acoustic horn in contact with the surface of the structure. The acoustic horn emits acoustic energy in the 10-50kHz range having a pulse energy in the range of 500-3000 Joules[7] for a duration of less than one second. As the structure begins to vibrate, frictional forces inside the cracks begin to heat the surrounding material. The process has proven to be a very good indicator of cracks within a panel; however, this method has weak detection rates with flaws other than cracks.

Like many other nondestructive techniques, thermography is often only qualitative. The entire surface of the structure must be inspected, where the flawed regions will differentiate themselves from damage free regions. There are many possibilities for this technique in the areas of composites. Delaminations as well as hairline fractures on the surface of the structures have been successfully detected using these methods. Much progress has already been made in this area and proves to be more useful every day.

### 3.3 SHEAROGRAPHY

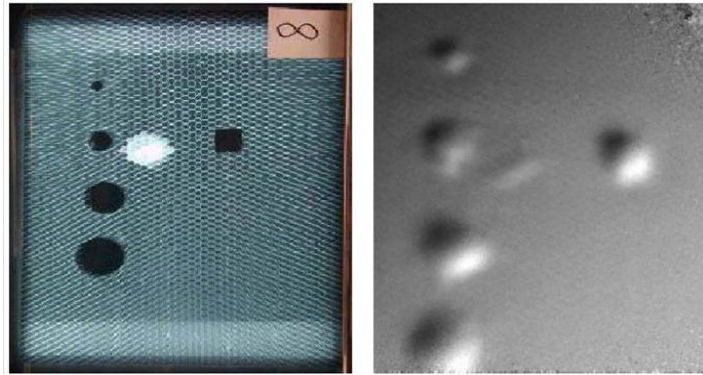


Figure 3.11 Image of a metal to metal bonded aluminum honeycomb structure containing pocket damages produced using X-Ray(left) and optical shearography(right) obtained from [9]. The high intensity white region shown in the X-Ray image is an unknown damage

Another popular optical, non-contact method is shearography; digital speckle shearography is starting to make its way into nondestructive evaluation. It is an interferometric method which uses images obtained from a structure while at rest and while loaded. These images, however, are not any ordinary image. They are obtained using a special camera which has a thin glass wedge which covers half of the lens. When the surface of the structure is illuminated by the laser, the camera produces two sheared images which interfere with each other producing a speckle pattern[9]. These images are obtained while the structure is at rest and loaded using the same high resolution film, where the speckle pattern will change while the structure is loaded. The two speckle patterns interfere with each other, revealing a macroscopic fringe pattern which correlates to the stiffness of the material. However, this fringe pattern is only visible using a high-pass Fourier filtering technique. With some further image processing techniques used to smooth out the image, damages such as pores, delaminations, and cracks become easily visible in the resulting image [9].

Fig. 3.11 displays an X-ray image along side of a shearographic image obtained from the

same honeycomb panel. As shown on this image, the defects in this honeycomb structure show up very clearly. These images were produced in the referenced work [9], which specialized in the development of a mobile scanning system to facilitate in-service inspection. With the development of a mobile scanning system, this method is a very effect flaw detection technique. It produces very detailed information about the structure which can be used for even more than flaw detection.

### 3.4 LOW FREQUENCY TECHNIQUES

#### 3.4.1 TAP TEST

The tap test is one of the simplest inspection techniques and often serves as the first line of defense when looking for flaws in honeycomb structures. The method only requires a coin and a good sense of hearing. As the surface is impacted with the coin, it emits a sound which is dependent upon the local stiffness. When a tap occurs over a flawed region, where the local stiffness is lower, the sound is dampened producing a “dead” tone, compared to a tap over an undamaged region which produces a higher tone [10]. With this simple method, technicians are able to quickly identify major flaws requiring further inspection of the structure.

This technique serves as a good initial examination to identify major flaws, yet it lacks the sensitivity of the other procedures. The dependence on the human ear introduces another variable, where some technicians may be able to identify smaller flaws than others. Eliminating the dependence on the human ear and instrumenting this technique would make it far more accurate and dependable. A system to perform this has previously been developed and is called the Computer Aided Tap Test(CATT) system. The technique is described in greater detail in Chapter 5.

### 3.4.2 MECHANICAL IMPEDANCE

The mechanical impedance,  $Z$ , of a system is defined as its resistance to motion [12]. In equation 3.1,  $F$  is the force applied,  $v$  is the resulting velocity of the point at which the force

$$Z = \frac{F}{v} \quad (3.1)$$

was applied, and  $Z$  is the mechanical impedance. Much like the tap test, mechanical impedance makes use of the change in stiffness a damaged region causes. The mechanical impedance of a damaged region will be lower than that of a non-damaged region, and decreases even further with increasing defect size. There exists a nondestructive method known as Mechanical Impedance Analysis (MIA) which makes use of this structural property. Mechanical impedance, however, is not measured using a single impact similar to that of the tap test; it is measured while the structure is being continuously excited at a set frequency.

The MIA probe consists of two separate piezo-electric crystals attached to a probe which makes contact with the surface of the structure[13]. The first piezo-electric crystal converts an electric signal into vibrations which are transferred to the structure surface. The second piezo-electric crystal is measuring the vibrations on the structure surface. It converts these vibrations back into an electric signal. The two crystals are stacked on top of each other, with the crystal sensing the vibrations of the surface stacked next to the surface. The crystals are made to operate at low frequencies, around seven kilohertz. The MIA probe is continuously vibrated at a set frequency during inspection. The difference between the induced vibrations and the measured vibrations is recorded. There should always be a slight difference between these two vibrations; therefore, before inspection, the probe is set on a good region of the structure and the difference between the two vibrations is measured and set as a baseline. A flaw in the structure would cause the difference in vibrations to change from that of a good region. If the difference between the vibrations stray too far from the baseline during inspection, the MIA method will identify that point as a flaw.

This method is able to detect delaminations very well, which can be explained by inspecting how a delamination affects a vibrating structure. A delamination creates a buffer zone between the material above and below it. When there is a delamination present, only the mass



above the delamination will vibrate, the delamination will dampen out much, if not all of the vibrations propagating through it. Therefore there is less vibrating mass in the damaged region in comparison to the mass in a non-damaged region. This mass is what gives the structure the resistance to motion; hence, less mass will result in less resistance to motion. Referring back to equation 3.1, this effect results in a higher velocity for the same applied force, which produced a lower mechanical impedance,  $Z$ .

## CHAPTER 4. IMAGE PROCESSING

Throughout the course of this research, many C-scan images have been generated on honeycomb composite panels using air-coupled ultrasonics. In nearly every case, the resulting ultrasonic image contained many regions of high transmission amplitude, which were in a honeycomb pattern. It was later found that these regions of high transmission amplitude were caused by the double walls of the honeycomb cells. Unfortunately, these regions of high transmission amplitude would make the resulting images very cluttered, and has the tendency to conceal flaws in the honeycomb composite. It was decided to take a slight detour from the main subject of this research to develop a process to be used to eliminate these repeated patterns from the images. A code was developed which made use of the a two dimensional spatial Fourier Transform to filter the image and reduce these patterns. Using this code as a post-processing routine, many of these honeycomb patterns could be reduced or even eliminated, allowing the flaws to be more visible.

### 4.1 FOURIER TRANSFORMS

The Fourier Transform is an extremely powerful tool used in signal processing and image analysis. The purpose of a Fourier Transform is to separate a signal into its frequency components. It transforms the x axis of a signal from the spatial domain to the spatial frequency domain, where the y axis will then represent the amount of the corresponding frequency component present in the signal. Fourier transforms are difficult to interpret when looking at the complex components representing the signal content. Complex numbers can be represented using either their magnitude or phase, the difference between these two representations will be discussed later.

$$F(u, v) = \sum_{x=0}^N \sum_{y=0}^M f(x, y) e^{-2\pi j \left( \frac{ux}{N} + \frac{vy}{M} \right)} \quad (4.1)$$

$$f(x, y) = \sum_{u=0}^N \sum_{v=0}^M F(u, v) e^{2\pi j \left( \frac{ux}{N} + \frac{vy}{M} \right)} \quad (4.2)$$

One dimensional Fourier Transforms are fairly common in signal processing analysis, where as their counterparts, two dimensional Fourier transforms, are not nearly as well known; yet, these two methods are very similar. Equations 4.1 and 4.2 represent the forward and inverse two dimensional Discrete Fourier Transforms respectively.  $F(u, v)$  is a function in the spatial frequency domain and  $f(x, y)$  is a function that resides in the spatial domain. The position components are  $(u, v)$  and  $(x, y)$  and N and M represent the total number of points in their respective axis. The forward transform will convert an image in the spatial domain to the spatial frequency domain and the inverse transform will convert an image back to the spatial domain from the spatial frequency domain. The two dimensional transforms only differ from the one dimensional transforms in the addition of a second summation which sums the extra variables, y and v, associated with the second dimension of the function. The derivation of equations 4.1 and 4.2 are not the subject of this section; however, they are outlined in Ref. [14]. The purpose of this section is to outline the applications of the two dimensional Fourier Transforms and introduce a written code which makes use of this technique to dramatically reduce the effects of the double walls in honeycomb composites on the resulting C-scan images.

The physical meaning of the two dimensional Fourier Transform is spatial frequency. It has the ability to draw out patterns in the image, where the more frequent a pattern is, the more noticeable it is on the resulting Fourier Transform. When referencing equations 4.1 and 4.2, the object of the summation may present confusion. Certainly an image is not a function dependent upon x and y, it is a factor which is observed with the eye. However, when a computer monitor or television screen displays an image, it breaks the image into many tiny pixels. Each pixel can emit one color, which has a numerical value ranging from 0 to 255. The object of summation in the Fourier Transform are these pixel values. The function simply becomes the value of the pixel at the location x,y or u,v. The classical representation of

a Fourier Transform involves an integral; although, the above equations have been modified to accommodate discrete data. They are Discrete Fourier Transforms specifically tailored to image processing.

Fourier Transforms attempt to represent an image as the sum of many cosine waves propagating in every direction, where the center of the image is the origin of each wave and the resulting frequency coordinate system [15]. The  $u$  and  $v$  variables represent the horizontal and vertical axis respectively. The center point, or the start of each cosine wave, is the mean value of all the pixels in the spatial domain image. This feature can be used to change the intensity of the entire image, where modification of only the center pixel will have an effect on every pixel in the resulting spatial domain image after the inverse Fourier Transform is taken.

#### 4.1.1 MAGNITUDE VERSUS PHASE REPRESENTATION

When a Fourier transform is performed on an image containing all real numbers, complex numbers are produced; therefore, the method used to display these numbers is either a magnitude representation or a phase representation. The equations used to calculate magnitude and phase are outlined in equations 4.3-4.5, where  $a$  and  $b$  represent the real and imaginary components of the complex number respectively.

$$F(u, v) = a + bj \quad (4.3)$$

$$\text{Magnitude}(F) = \sqrt{a^2 + b^2} \quad (4.4)$$

$$\text{Phase}(F) = \tan^{-1} \left( \frac{b}{a} \right) \quad (4.5)$$

The magnitude will represent how much of a frequency component is present while the phase will symbolize the location that frequency component is occurring [15]. Magnitude plots are the most common method of displaying the Fourier Transforms; they tend to provide more usable information. The code developed throughout this research made sole use of magnitude

plots; therefore, only the magnitude representation will be discussed for the remainder of this section.

## 4.2 IMAGE ANALYSIS

There is no better way to explain a two dimensional Fourier Transform than to simply inspect its results. Several images have been processed and are shown with their corresponding spatial frequency domain image, attained using the two dimensional Fourier Transform. Two images are displayed in Fig. 4.1. The top left image is composed of horizontal lines, which form a pattern in the vertical direction. The spatial frequency domain image represents this pattern as two high intensity dots located on the vertical axis. The distance these dots are located from the origin is dependent upon the period of the pattern. If the pattern is highly frequent, the dots will be further away from the origin.

Below the bottom left image is an identical the top left image, but rotated 90 degrees. The corresponding spatial frequency domain image is then also rotated 90 degrees, containing dots now on its horizontal axis. These two images contain very simple patterns and as a result their Fourier Transforms are also very simple; this however is not always the case. As more patterns are added, the Fourier transform becomes more complicated.

Fig. 4.2 shows a spatial domain image which is much more complicated. At first glance, the image is obviously in color rather than gray scale. Color images contain three separate values for each pixel, which correspond to the red, green, and blue color components. This simply means there is more data contained in the spatial domain image hence, more data for the Fourier Transform to process. There are also three different patterns contained in the spatial domain image, which cause three different effects in the spatial frequency domain.

As opposed to the previous images, this image does not have smooth, cosine-like, transitions in its patterns; it is composed of solid lines with sharp edges much like step functions. In order for the Fourier Transform to represent these sharp edges, many frequency components are necessary. In the resulting spatial frequency domain, rather than having intense isolated points, these sharp edges cause lines in the image. This effect can be seen on the right, where

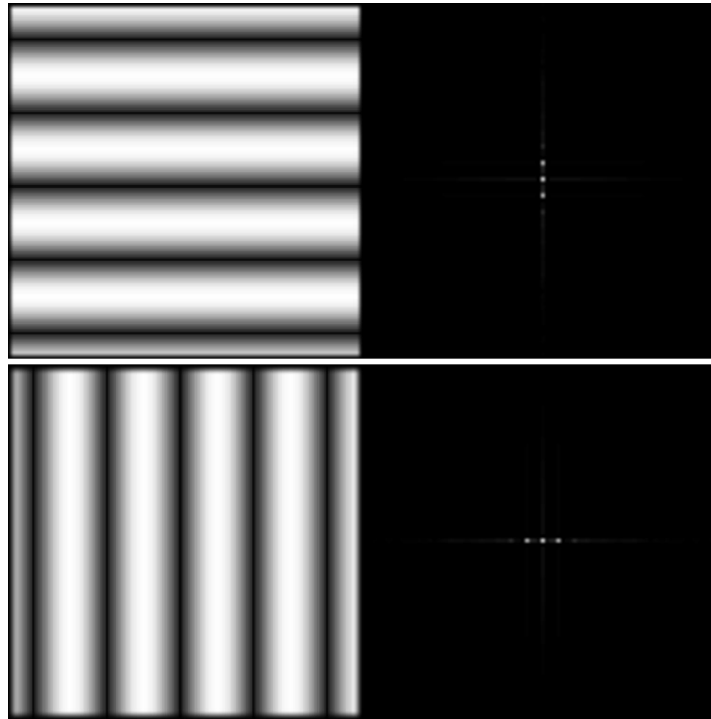


Figure 4.1 Two dimensional Fourier Transform two images: Top-image containing a vertical pattern which show up in the FT as dots along the vertical axis, Bottom-same image only rotated 90 degrees, now the dots form on the horizontal axis in the resulting FT image

the resulting effects in the spatial frequency domain form what seem to be dotted lines.

The effect of color in the spatial domain image can facilitate a better understanding of the spatial frequency domain image. The red lines in the spatial domain image cause effects in the spatial frequency domain image which also have a red color. This relation can make it easy to distinguish the features in the spatial domain image to the effects they have on the spatial frequency domain image. Also, the color in the images can be advantageous when attempting to eliminate the patterns in the image.

Fig. 4.3 shows an example of the Fourier transform of an image containing many frequent patterns. The image is a C-scan performed using ultrasonic transduction on a honeycomb composite panel. The bright red dots covering the image are caused by the double walls in the honeycomb, where more sound transmitted through the panel. This particular image displays

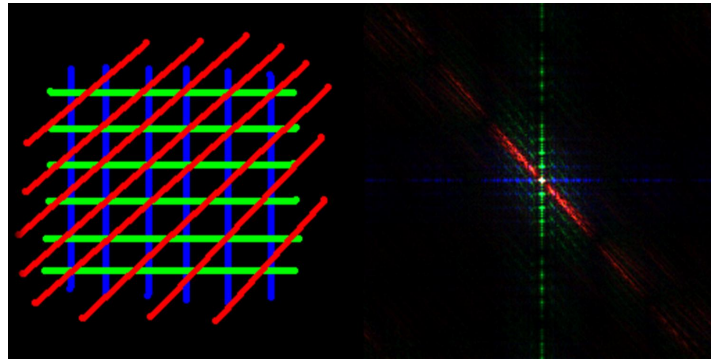


Figure 4.2 Two dimensional Fourier Transform of an image in color

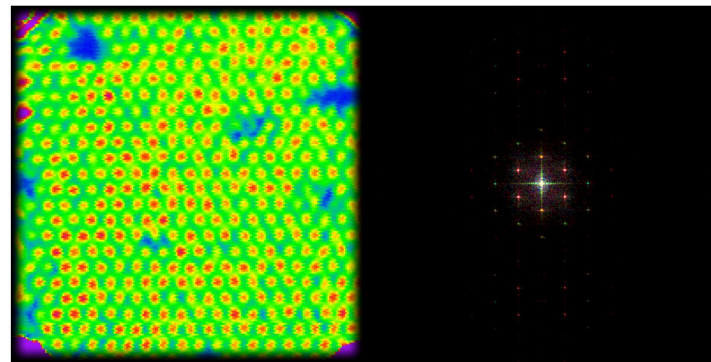


Figure 4.3 Two dimensional Fourier Transform of a C-scan image of a honeycomb composite panel. Left: Spatial domain image, Right: Spatial Frequency domain image

the need for image processing due to the frequent patterns caused by the double walls of the honeycomb. These frequent patterns, seen in most C-scan images on honeycomb composites, are very distracting. Many times flaws can go unnoticed as a result of these distracting patterns.

The red dots in the spatial domain cause high intensity points, which contain a reddish tint surrounding the origin of the spatial frequency domain. There are several spatial frequencies present in the honeycomb pattern displayed by the red dots; for this reason, there are several dots in the spatial frequency domain, each representing one frequency associated with the pattern in the spatial domain image. As long as the patterns can be identified in the spatial frequency domain, steps can be taken to eliminate these features from the spatial frequency domain and then, by taking an Inverse Fourier Transform, producing a spatial domain image which would be free of these distracting patterns.

### 4.3 FILTERING

Filtering in the spatial frequency domain is relatively simple. There are several techniques which can be used which all have differing effects on the spatial domain image. The simplest form of filtering involves focusing on each individual high intensity point in the spatial frequency domain and eliminating it. By averaging the center pixel of the intense region with all surrounding pixel values and replacing the center value with the average, the high intensity point is eliminated; however, the process may need to be repeated several times before the high intensity point is fully eliminated. This can be performed not only on the center pixel value, but also on many of the surround pixel values. The high intense region will slowly start to fade away as the average of all the points becomes constant.

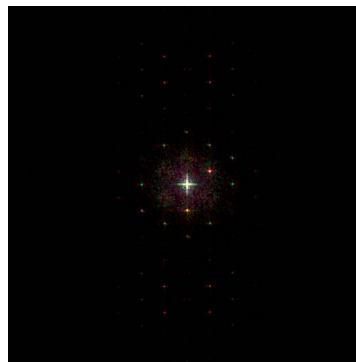


Figure 4.4 Initial filtering with high intensity points smoothed over

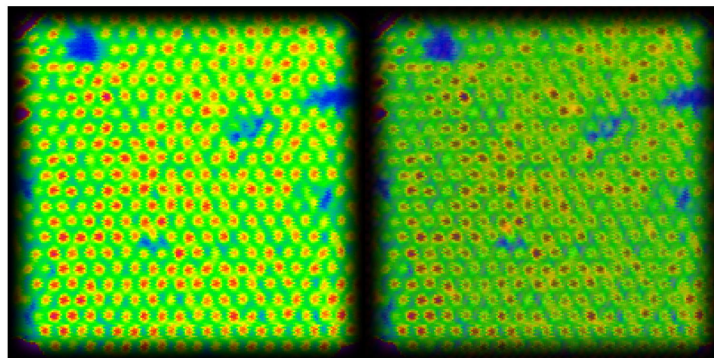


Figure 4.5 Resulting inverse Fourier Transform of Fig. 4.4: Left-Original image, Right-Filtered image



Fig. 4.4 and Fig. 4.5 show the effects of point smoothing. In Fig. 4.5, the original image is shown on the left and the corresponding filtered image is shown on the right. Although the high intensity points are still very visible, they are beginning to be removed from the image. Only a few points were smoothed in the spatial frequency domain, and the effects already begin to show in the spatial domain image.

Another very useful filtering technique is the low-pass filter. Often it is very hard to individually select all the high intensity points on an image when some points may not stand out to the extent of the others. This low-pass filter sets all the points which exceed a specified radius from the origin equal to zero, eliminating all high frequency content. If the high intensity points are very far away from the origin, this technique can be very effective.

One drawback to low-pass filtering is that it has the effect of blurring the image. As discussed earlier, very sharp edges require a lot of high frequency content to generate. If all high frequency content is eliminated, the Fourier Transform no longer has the ability to represent the sharp lines. The contour lines in the resulting filtered image become more gradual, which, in effect, blurs the image.

Finally, the last technique to perform makes use of the colored image. We can reduce the intensity of only the red color to further reduce the visibility of the honeycomb pattern in the image because the high intensity points are red. Fig. 4.6 and Fig. 4.7 show a Fourier Transform and its resulting Inverse Fourier Transformed which were optimized to reduce the effects of the honeycomb as much as possible.

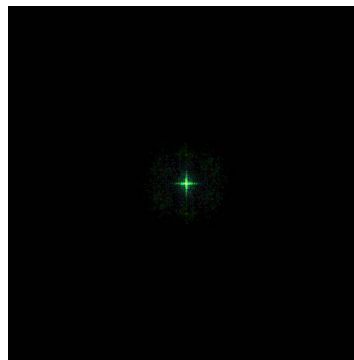


Figure 4.6 Filtered spatial frequency domain image using point smoothing, low-pass filter, and red reduction

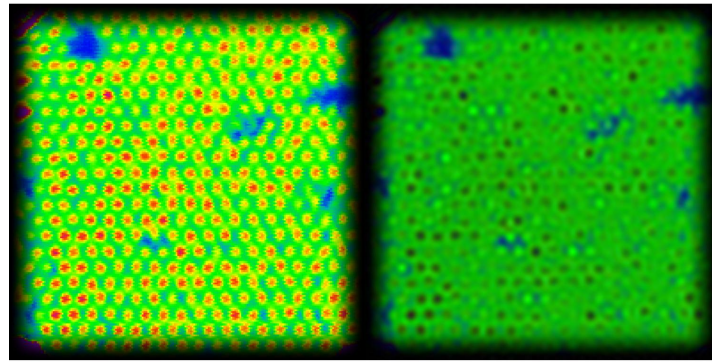


Figure 4.7 Resulting inverse Fourier Transform of Fig. 4.6: Left-Original image, Right-Filtered image

#### 4.4 PROGRAM

The program used to generate all the previously shown Fourier Transforms was written throughout the course of this research by the author. A mathematics package called Promath4 [16] was used to perform the two dimensional Fourier Transforms for all images. The program is titled, “2D FFT Image Cleaning,” and is displayed in Fig. 4.8. This figure shows the console of the program as well as an original image displayed on the right, where all image processing begins.

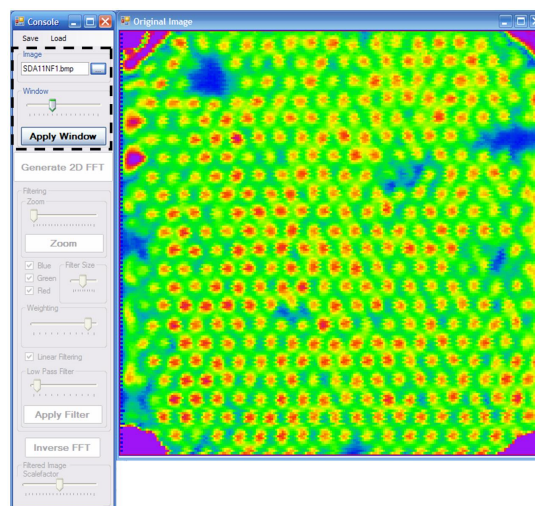


Figure 4.8 2D FFT Image Cleaning Program: Console and Original Image

Processing begins with the opening of an image and the application of a window to it. The window reduces the edge effects on the original image. Again, these edges act like step functions. The window will turn this step function into a cosine function. Although some of the information in the original image is lost, it reduces a strong cross pattern which appears at the center of the resulting spatial frequency domain image due to the shape edges of the spatial domain image. Windows are applied using the slider bar on the top portion of the console, outline in Fig. 4.8. Once a proper window is selected, the “Apply Window” button is clicked and the windowed image is generated. The results of this process are shown in Fig. 4.9, where the edges of the windowed image now taper off to a uniform zero value region.

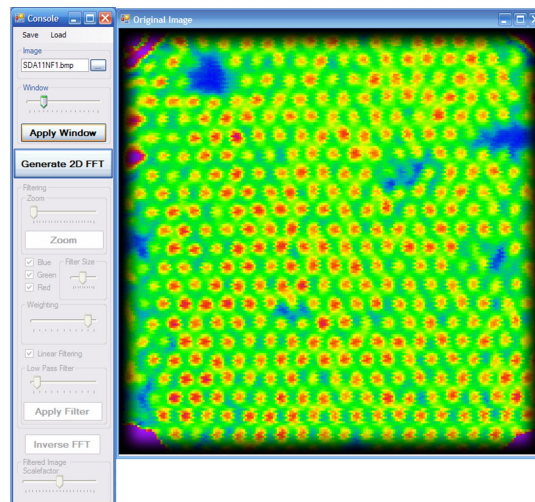


Figure 4.9 2D FFT Image Cleaning Program: Windowed Image

The next step is to generate the Two Dimensional Fourier Transform, which is performed by clicking the “Generate 2D FFT” button. FFT is an acronym for “Fast Fourier Transform,” where the only difference between the FFT and the FT is an algorithm, which speeds up the Fourier Transform process. FFTs greatly reduces the number of computations needed to produce the spatial frequency domain image.

The spatial frequency domain window has several sub windows which each display a different image. The larger image on the right of the window is the complete spatial frequency domain image. Next to the complete spatial frequency domain image are the three images on

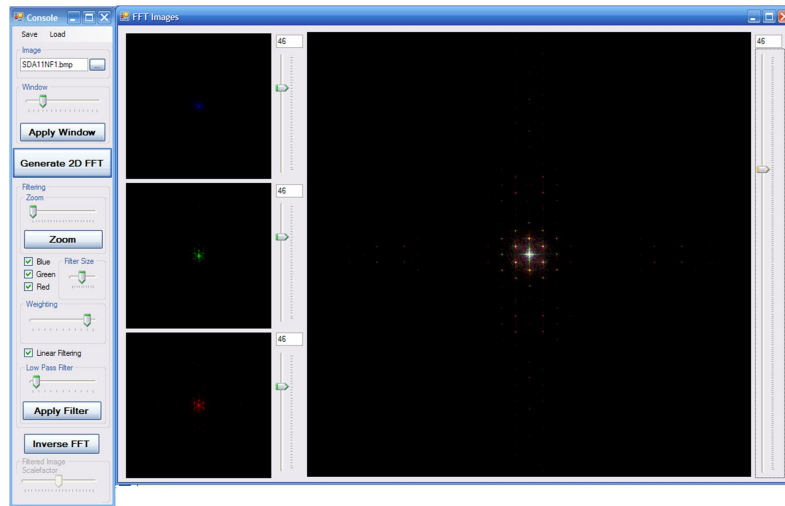


Figure 4.10 2D FFT Image Cleaning Program: spatial Frequency domain Image

the left of the window which are the separate color components of the complete image. The complete image is on a red, green, and blue scale; therefore, the left images show the red, green, and blue components of the complete image. Along the right border of each image is a slider bar which controls the brightness of the corresponding image. The slider bar of the complete image will increase the brightness of all three color components on its left. The slider bars of each individual color component will only increase the brightness of its corresponding color component. This can be used to reduce specific color components which relate to frequent patterns.

Once the Fourier Transform has been performed, several features become active on the console. The first feature is a zoom function that allows the user to zoom into the Fourier Transform. This is very useful when low frequency patterns are present in the image because these patterns will cause high intensity points close to the origin; a zoom function may be necessary to properly filter the image. The zoom function contains a slider bar and a zoom button. The slider bar controls the magnitude of the zoom and displays a white box on the image to show the area to be magnified.

Below the zoom button is a region which contains a series of three check boxes beside a slider bar controlling the filter size. The functions control the properties of a feature used

to eliminate the individual high intensity point on the spatial frequency domain image. This feature is performed by placing the cursor over and clicking directly on the high intensity points in the spatial frequency domain image. When a point is clicked, a nine point average is taken of the center pixel and the eight surrounding points. The center pixel is then replaced with this average value. The red, green, and blue check boxes represent which color components are being filtered; if a box is left unchecked, that corresponding color component will not be filtered. The filter size sliding bar represents how many pixels will be replaced with average values. The slider bar controls the radius of a circle with its center located on the pixel which was clicked; every point which falls inside of this circle is replaced by its surrounding nine point average. If the filter is set to the far left, only the center pixel will be filtered; however, as the filter slides to the right, this process will be repeated for the every point which falls inside the circle. As the slider bar moves right, more pixels will be replaced with their surrounding nine point average.

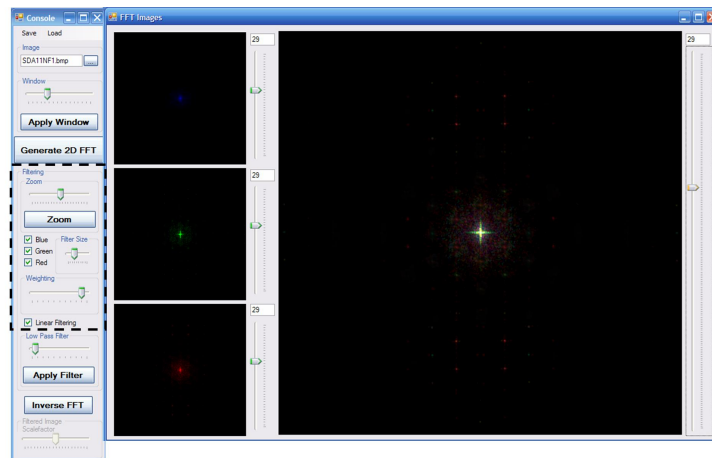


Figure 4.11 2D FFT Image Cleaning Program: Point Filtering

There are two more features which effect the properties of this filtering technique. Below the region previously discussed is an additional slider bar. This slider bar controls the weighting of the nine point average every time a point is clicked. As the slider bar slides farther to right, the more weight is put on the center pixel. If the slider bar is at its right-most position, there is no longer any averaging being performed, as all the weighting is on the center pixel. There is

also a check box below this slider bar called “linear filtering” which has the ability to eliminate several points with a single click.

The spatial frequency domain image is a symmetric image about both the u and v axis. Also, because the Fourier Transform attempts to represent the image with many cosine-like waves, these high intensity points will be repeated along every multiple of the period of the cosine wave. On the spatial frequency domain image, this is shown by several points radiating from the origin. The points closest to the origin are the highest intensity and as the distance increases the points become less intense. The linear filtering feature makes use of this Fourier Transform property. If this box is clicked, not only will the current point be filtered, but also several other points which correspond to the repeating pattern of the cosine wave. The distance in between each point corresponds to the period of the cosine wave used to approximate the original high intensity point. Because the cosine waves originate at the origin, all these points are located on the same line radiating away from the origin in both directions. When a point is clicked, its distance from the origin is the period of the cosine wave. This feature makes use of this property and is able to approximate the location of several other points caused by the same pattern and filters those points as well. Fig. 4.11 shows a filtered spatial frequency domain image using this point filtering technique along with the zoom feature.

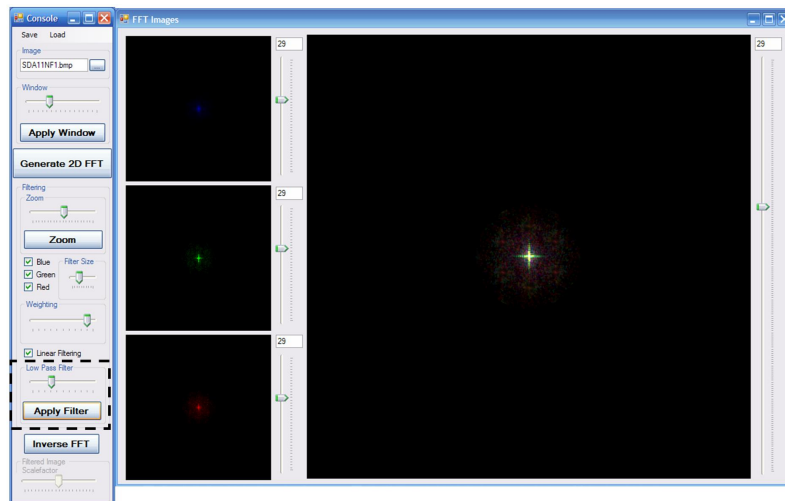


Figure 4.12 2D FFT Image Cleaning Program: Low Pass Filter

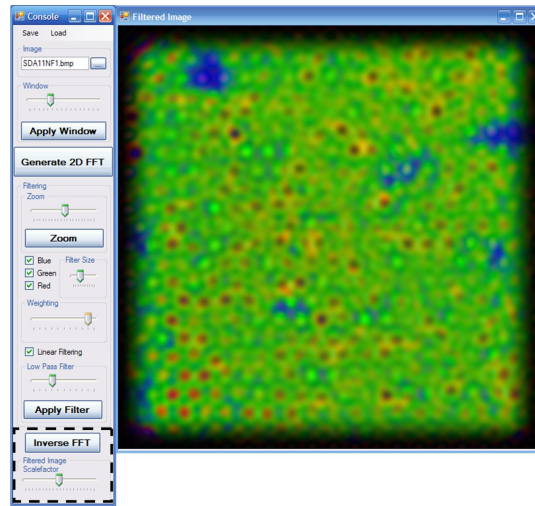


Figure 4.13 2D FFT Image Cleaning Program: Inverse Fourier Transform

The final form of filtering is the low pass filter. Below the linear filtering check box, there is a slider bar which controls the size of the low pass filter. The size of the filter is displayed on the spatial frequency domain image visually, showing up as a white circle; everything outside of this circle will be filtered out of the image. After the filtering is complete, the Inverse Fourier Transform can be performed by clicking the “Inverse FFT” button. The Inverse Fourier Transform converts the image back to the spatial domain, where the original image was displayed.

There is one final form of image processing which can be used on the filtered spatial domain image. This is simply a brightness adjustment, which is controlled using the slider bar directly below the “Inverse FFT” button. However, many times this feature is not required. There are also extra features on the console which allow you to save and load the spatial frequency and spatial domain images. This program has proved to be very useful when using ultrasonic transduction to scan honeycomb composite panels due to the effects the double walls have on the resulting C-scan image.

## CHAPTER 5. COMPUTER AIDED TAP TEST

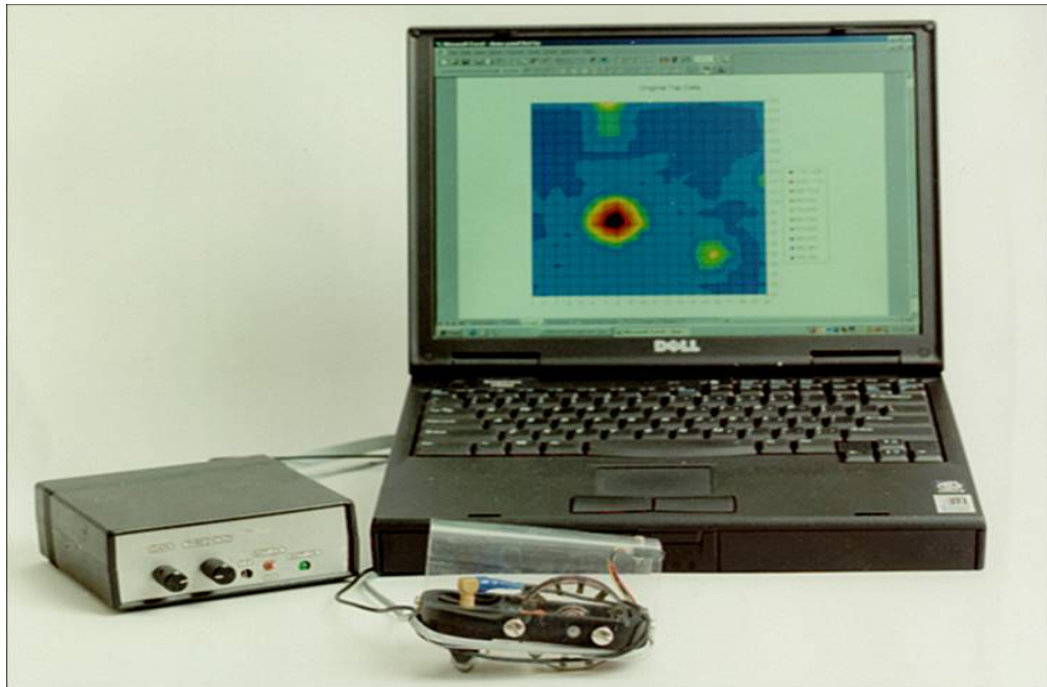


Figure 5.1 Computer Aided Tap Testing System

The Computer Aided Tap Test (CATT) is a method which makes use of an accelerometer and electric circuit to capture the impact duration,  $\tau$ , of the tap. It has been shown that the impact duration, as well as the tone of the tap, correlates with the local stiffness. The CATT system is able to store these  $\tau$  values and plot very informative contour maps over the surface of the structure. Fig. 5.1 shows all components of the CATT system as well as an example of a CATT image produced on the computer screen. The photo also shows a magnetic cart in the foreground, which provides a quick, semi-automatic method of obtaining all the  $\tau$  values over the surface of the structure.



The CATT system is a major improvement to the manual, hearing-based tap test. It has the ability to store the tap data of each structure and holds a finer and more uniform inspection sensitivity. The theory and applications of the Computer Aided Tap Test system can be used as a tool for quantitative nondestructive evaluation. The material discussed in this section is not an original work; however, the hysteresis method, which is the main topic of this thesis, is heavily dependent upon this method. The discussion that follows was taken from the referenced work [10].

## 5.1 THEORY

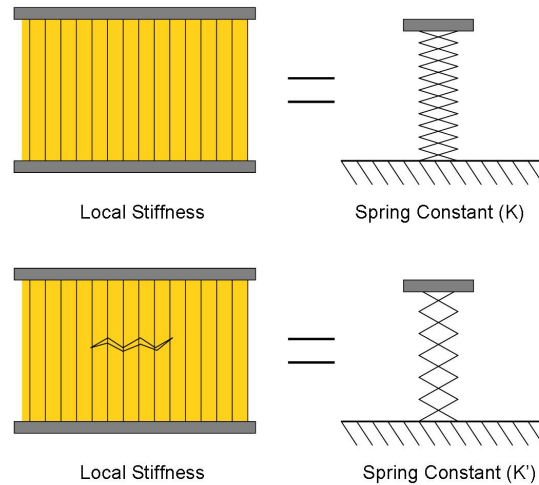


Figure 5.2 Honeycomb composite structure approximated as a grounded spring having a spring constant of  $k$

A composite structure can be approximated by a grounded spring with a spring constant of  $k$ , where the local stiffness of the structure is directly related to the spring constant. If an undamaged region has a stiffness of  $k$ , then damaged region would have a lower stiffness of  $k'$ , as shown in Fig. 5.2. This causes the changed tone of the sound emitted from the structure when it is tapped. One of the challenges in developing the CATT system was to isolate the variable  $\tau$ , which also correlates well with stiffness and so that it can be easily measured. Using an accelerometer to measure the acceleration of the tap showed promise for finding a variable

which could be measured and stored. The local stiffness of the structure will have a large effect on the acceleration of the tap.

### 5.1.1 ACCELEROMETER SIGNAL OUTPUT

The accelerometer is the key component of the CATT system. A round tip is mounted on the end face of the accelerometer which is used to make contact with the surface of the structure. In order to take an in-depth look at the theory behind the CATT system, the role of the accelerometer and the acquired tap signal must be clearly understood.

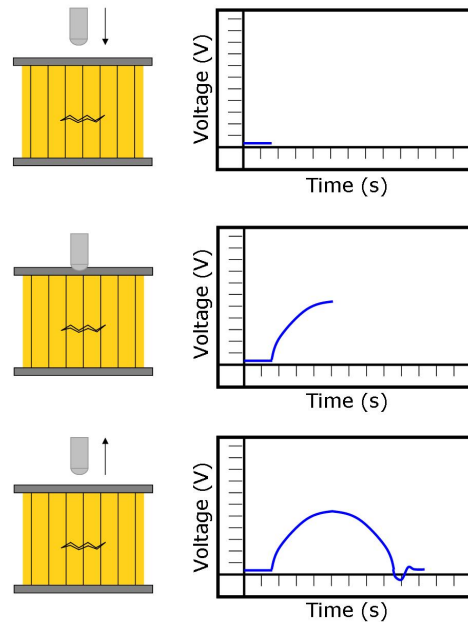


Figure 5.3 Accelerometer signal output

Fig. 5.3 shows a typical signal output of an accelerometer from a tap. As the tapper mass compresses the structure, the instantaneous acceleration increases to a maximum, corresponding to the point of maximum deflection of the surface of the structure. As the structure begins to return to its original shape, it begins to accelerate the accelerometer in the opposite direction, decreasing the acceleration from the initial maximum and then tapering off until the accelerometer is no longer in contact with the surface. A slight asymmetry with respect to time is often observed in the signal output of the accelerometer. This asymmetry is usually

small and the signal output can be modeled approximately as the half cycle of a sine wave in the grounded spring model below (Sec. 5.1.5).

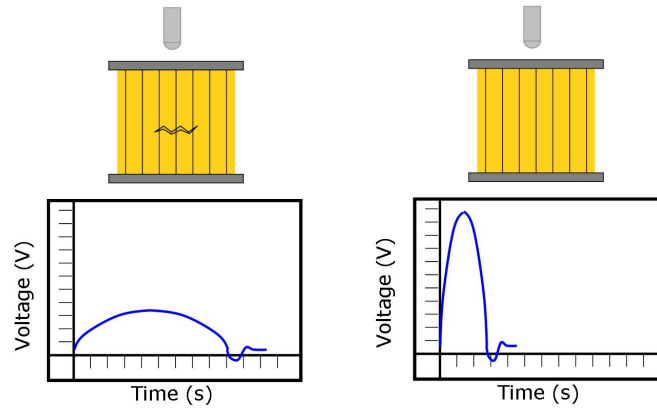


Figure 5.4 Effect of a flaw on the accelerometer signal

### 5.1.2 EFFECTS OF DAMAGE

A flaw in the composite affects the signal output of the accelerometer. Fig. 5.4 shows the general trend typically produced when a tap occurs over a flawed region. The acceleration curve commonly has a lower maximum acceleration and a longer impact duration. The curve appears to be compressed vertically and stretched horizontally. Either of these two parameters could be used to differentiate a damaged region from an undamaged region, though impact duration proved to be a more stable and easily measured parameter. The amplitude of the acceleration depends strongly on the force used in the tapping, but the impact duration is largely independent of the tapping force.

### 5.1.3 EFFECTS OF IMPACT FORCE

When using the magnetic cart, impact force can be considered relatively constant; still, if a manual tap method is used, the operator must impact the structure by hand using the tapper to strike the surface of the structure. For this reason, impact force cannot be considered a constant. The effects of varying impact force are shown in Fig. 5.5 for undamaged and damaged

regions. The tests were performed on a composite honeycomb panel from NWA (B747 trailing edge flap). The impact damage was induced by dropping 1.5" diameter ball bearing from a height of 10 feet. The impact duration,  $\tau$ , is seemingly unaffected by the magnitude of the tap force. By relating the result with the period of a simple harmonic oscillator (e.g. an oscillating spring or a swinging pendulum), this phenomenon can be understood.

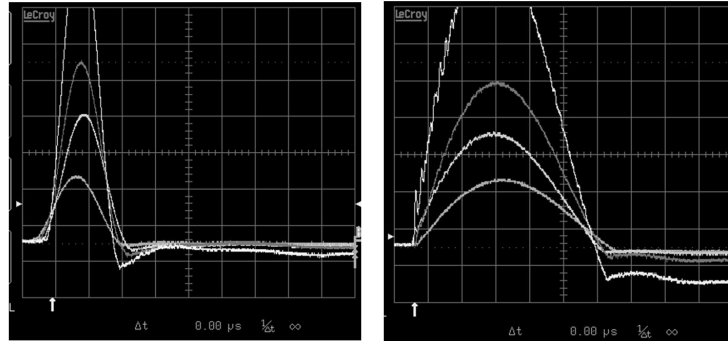


Figure 5.5 Accelerometer signal output at an undamaged region(left) and a damaged region(right), representing soft, medium, and hard tap forces for each case. The impact duration(contact time) of all three curves was about  $250\mu s$  for the undamaged and  $500\mu s$  for the damaged region

A swinging pendulum will have the same period despite its swing amplitude. This also holds true for a grounded spring which simulates the stiffness of a honeycomb sandwich structure. For a grounded spring model, the impact duration is independent of the initial spring compression, which can also be related to the initial impact velocity of the tapper. This behavior is crucial to both the CATT system as well as the hearing-based tap test since the tap force does not need to be controlled.

#### 5.1.4 GRESZCZUK'S EQUATIONS

The impact between an accelerometer and a flat surface can be described mathematically as well, without using the approximation of the acceleration curve as a half cycle of a sine wave. Equation 5.1 was derived by L. Greszczuk for the impact duration,  $\tau$ , of a spherical impactor

on a flat surface[11]. In equations 5.1-5.5 for the tapper and the structure respectively,  $m_t$  and  $m_s$  represent mass,  $E_t$  and  $E_s$  represent Young's modulus,  $k_t$  and  $k_s$  represent stiffness, and  $\nu_t$  and  $\nu_s$  represent Poisson's ratio. Also,  $R_t$  represents the radius of the tapper and  $v$  represents the velocity of the tapper immediately prior to impact with the surface.

$$\tau = 2.94 \left( \frac{5}{4Mn\sqrt{\nu}} \right)^{\frac{2}{5}} \quad (5.1)$$

$$M = \frac{1}{m_t} + \frac{1}{m_s} \quad (5.2)$$

$$n = \frac{4\sqrt{R_t}}{3\pi(k_t + k_s)} \quad (5.3)$$

$$k_t = \frac{1 - \nu_t^2}{\pi E_t} \quad (5.4)$$

$$k_s = \frac{1 - \nu_s^2}{\pi E_s} \quad (5.5)$$

Other than the obvious dependence upon the material properties of the tapper and the structure, Greszczuk's equations show that  $\tau$  depends upon the mass of the tapper, the radius of the tapper, and the velocity just before impact. However, the dependence on radius and velocity is quite weak, requiring a large change in impact velocity to significantly change the value of  $\tau$ . This can be observed in Fig. 5.5 where a slight variability in the  $\tau$  values is present as the impact velocity increases. The variability in  $\tau$  is, then again, insignificant in relation to the change in maximum acceleration.

### 5.1.5 GROUNDED SPRING MODEL

The grounded spring model offers a simple method to relate  $\tau$  to the stiffness of the structure. As aforementioned, the structure can be approximated by a grounded spring having a spring constant  $k$ . The spring constant has a direct correlation with local stiffness, so  $k$  is referred to as local stiffness. The acceleration curve is taken to be half cycle of a sine wave, therefore  $\tau$  can be approximated by one half of the period of a sine wave. Equation 5.6 shows that  $\tau$  is proportional to  $m_t$  and the local stiffness, where  $f$  is the frequency of the sine wave,

$\omega$  is the angular frequency,  $m_t$  is the mass of the tapper, and  $k$  is the stiffness of the material. More specifically, the local stiffness is inversely proportional the the square of the  $\tau$  value; e.g. as the stiffness decreases  $\tau$  will increase. This result is commonly witnessed in experimental studies and also holds true when using Greszczuk's equations. Assuming the same tapper is used to tap the entire surface of the part,  $m_t$  will remain constant. If this is the case,  $\tau$  will only vary with the local stiffness. Equation 5.6 can be rearranged to solve for the local stiffness, shown in equation 5.7.

$$\tau = \frac{1}{2f} = \frac{\pi}{\omega} = \pi \sqrt{\frac{m_t}{k}} \quad (5.6)$$

$$k = \left(\frac{\pi}{\tau}\right)^2 m_t \quad (5.7)$$

An Imada loading frame and force gauge with a dial gauge attached to the loading frame are utilized when testing in order to measure load and displacement. From the load-displacement curve, the slope of the curve corresponds to the stiffness of the structure. A test comparing the mechanically measured local stiffness with the calculated stiffness from a tap was performed and the results are shown in Fig. 5.6. As Fig. 5.6 shows, when the calculated stiffness from a tap was compared to the experimentally measured stiffness using a load frame, the results represent nearly a direct correlation between the two. Tests were also performed on many different composite specimens made up of various composite materials with unique properties. The structures were tapped in several locations and the stiffness was measured in the same locations employing the use of the loading frame setup. A correlation between calculated and measured stiffness values is again nearly direct and adds validity to the assumptions made during the derivation of equations 5.6 and 5.7.

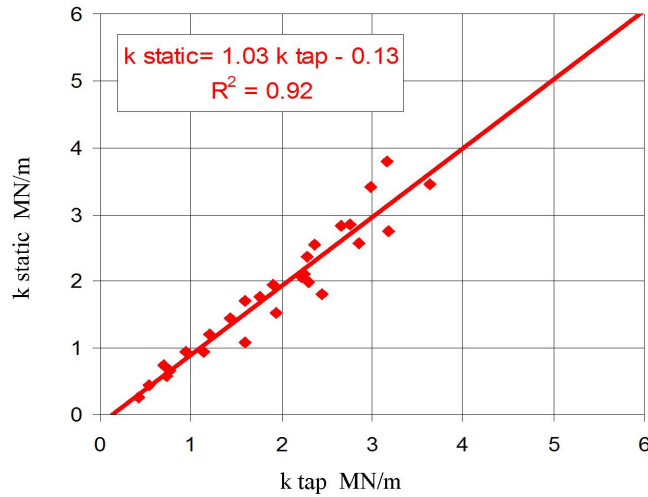


Figure 5.6 Experimental data showing the agreement between stiffness deduced from tap test data and stiffness directly measured in static loading tests

## 5.2 APPLICATIONS

The tap test is already used heavily in the field by technicians to quickly indicate if a part has damage. The CATT system can provide quick and easy visual data to determine if a part is due for repair. The strongest attributes of the CATT system are found in its simplicity and low cost. The CATT system is a fraction of the cost of most trusted nondestructive testing systems and it does not require in-depth knowledge of the system to operate. This system could efficiently be used by technicians in the field providing reliable data which can be stored within company records.

Fig. 5.7 highlights a B747 outboard spoiler(left) and its resulting tap test image(right). There are several crucial features present within the panel on the left that cannot be seen with the naked eye. When the CATT scan is completed, the image(right) shows many key characteristics, most notably the high stiffness region associated with the actuator fitting in the center of the panel. The ply build up to this region can also be seen in the image as well as the core spliced regions.

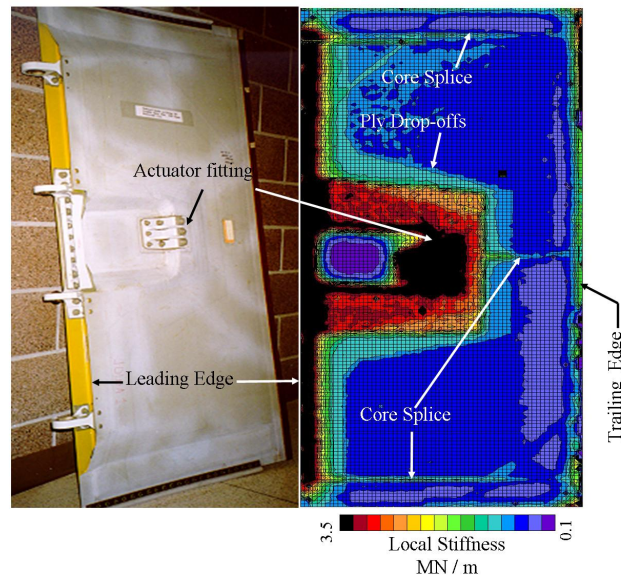


Figure 5.7 Tap test image of a B767 outboard spoiler, test performed on the flat side of the spoiler

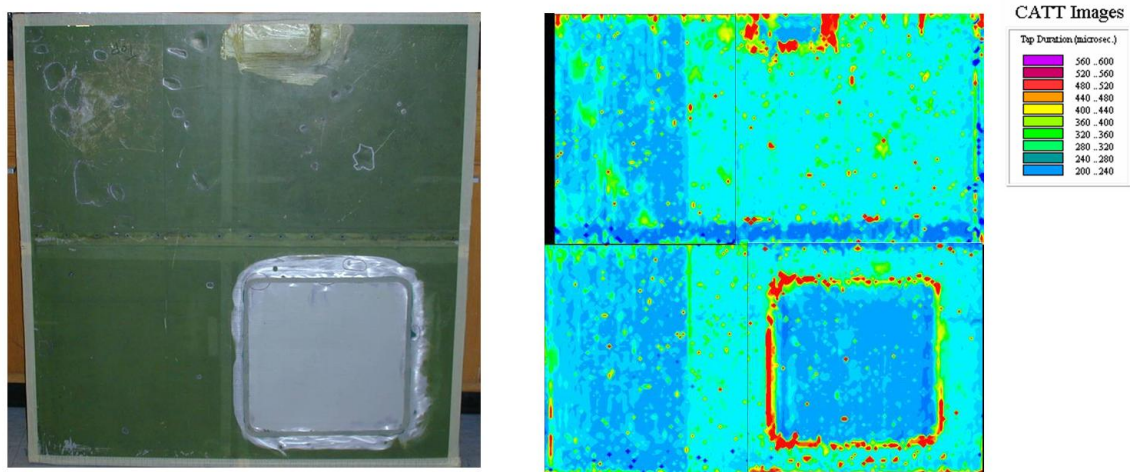


Figure 5.8 Tap test image of a C-5 Torque Deck

The tap test image of a heavily damaged C-5 torque deck panel is shown in Fig. 5.8, where flaws are circled in white on the surface of the panel. A tap test was conducted in an attempt



to detect these flaws. The image on the right of Fig. 5.8 is the tap test image, which shows that many of the features present on the panel are apparent in the tap test image. The level of severity of the damages can also be judged, with white corresponding to a severely damaged area. The bottom left box in both images is a repaired region of the torque deck. Repaired regions can easily be mapped out by the tap test because they almost always cause a stiffness increase. In addition, there are several other potential damages shown in the tap test image.

## CHAPTER 6. HYSTERESIS

### 6.1 WHAT IS HYSTERESIS

“Hysteresis is a property of systems (usually physical systems) that do not instantly follow the forces applied to them, but react slowly, or do not return completely to their original state: that is, systems whose states depend on their immediate history,” as stated in Wikipedia Online Encyclopedia.

The hysteresis phenomenon emerges in several places including electricity, magnetism, and mechanical systems. The hysteresis loop appears in the stress-strain curve of honeycomb composites where the stress is not only dependent upon the instantaneous value of strain but also the history of the loading phase. Each value of strain will correspond to two different values of stress, one being on the loading phase and the other on the unloading phase. This causes the loop effect, shown in Fig. 6.1, which is a strong indicator of hysteresis.

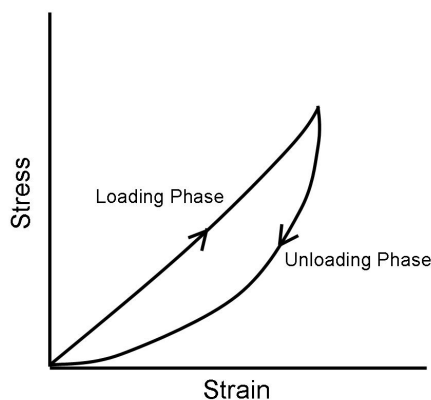


Figure 6.1 Typical stress-strain curve showing a hysteresis effect

It has been found during the course of this research that the area enclosed by the hysteresis

loop gives some indication to the level of damage in honeycomb composite materials. The physical meaning of the area enclosed by the loop is absorbed energy. More specifically, this is the energy absorbed by the structure due to internal frictional forces. When a crack or buckle develops in a honeycomb core, the number of surfaces where frictional loss can occur increases. Observing a crack, the level of frictional loss should increase dramatically due to fibers intertwining with each other when compressed and then having to untangle as the load is reduced and the structure returns to its original shape. Crack propagation can also be a reason for some of the absorbed energy. Integration of this property as a nondestructive technique would be useful; therefore, it will be beneficial to keep the energy delivered to the structure low enough to avoid crack propagation.

## 6.2 STATIC LOADING

When generating a stress-strain curve, structures may be loaded in two manners. Static loading, being one method, allows the structure sufficient time to adjust to the load, providing the maximum amount of frictional loss to take place. However, these tests take much longer to perform and are inadequate, from a time standpoint, when attempting to test the entire surface of a structure. The purpose for these static loading tests is to verify the theories, the correlation between loop area and damage, experimentally. Upon verification of these theories, the issue of slow loading times can be addressed and a dynamic loading setup can be investigated.

### 6.2.1 LOADING FRAMES

Fig. 6.2 shows a manually operated setup used to attain hysteresis loops. An Imada loading frame was mounted with both a force gauge and a dial gauge which were used to measure load and displacement respectively. The structures were incrementally loaded in steps. At each step the loading was halted and the structure was allowed time to relax, typically 30 seconds, before moving to the next step. Shortcomings with this setup include the requirement of manual loading using a crank on the loading frame. Manual recording of all data is also

required due to a lack of data storage features which leads to a large uncertainty in each data point due to the human factor in the tests.



Figure 6.2 Imada loading frame mounted with an Imada force gauge(bottom right) and displacement dial gauge(top right)

The second test setup makes use of an automated test setup called an INSTRON where the human factors were able to be eliminated. Fig. 6.3 and Fig. 6.4 display the INSTRON machine used for experimental tests. INSTRON tests proved to be pseudo static, but containing qualities of both dynamic and static loading. There was a very low loading rate( $0.003 \frac{mm}{sec}$ ) programmed into the INSTRON, where the INSTRON continuously moving acting much like a dynamic loading setup, yet its total loading time was closer to a static loading setup. This still allowed the structure sufficient time to relax even though the machine was continually changing the level of compression on the structure.

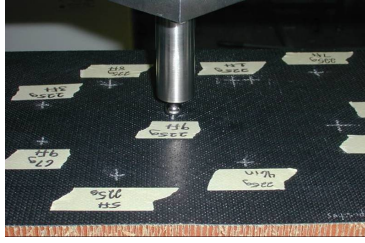


Figure 6.3 Sample bay on the INSTRON testing machine

### 6.2.2 TESTING FACTORS

Several factors come into play when using a static loading setup. During experimental tests it was determined that the size of the hysteresis loop was heavily dependent upon the time of the test. More specifically, it was dependent upon the step size and the loading rate; loading rate equals the time the structure was allowed to relax at each step. These two factors determine the length of the test.



Figure 6.4 INSTRON testing machine

### 6.2.2.1 STEP SIZE VARIATION

The structure used for the step size variation experiments is shown in Fig. 6.11. Fig. 6.5 and Fig. 6.6 illustrate the effect of a step size variation in the hysteresis loops and loop areas during static loading. As displayed in Fig. 6.6, the area under the loop begins to decrease as step size increases, although it begins to plateau at a step size of 20 Newton, where the area begins to remain constant. Evidence of this is depicted in the data points approaching the 10 newton step size and those preceding. The area of the 10 and 20 Newton step sizes are nearly the same where as during smaller step sizes the areas changed drastically.

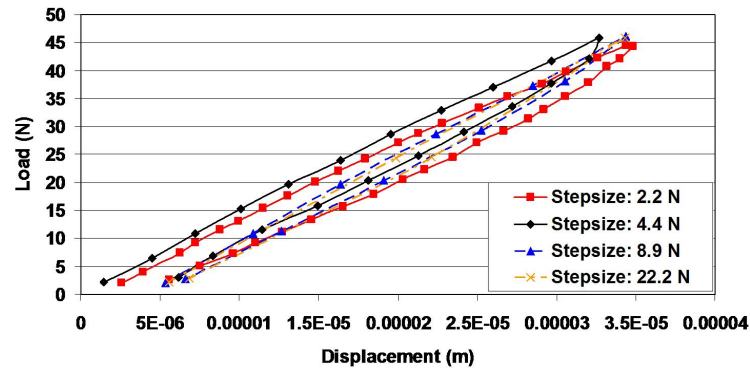


Figure 6.5 Effect of the step size variation on the hysteresis loops during static loading

The slope of the stress-strain curve remains constant with the changing step size. Loop area shows evidence to be the only parameter affected by step size and it is only affected up to a certain measured load. Larger step sizes will produce more consistent loop areas and eliminate the variability of loop area with changing step size.

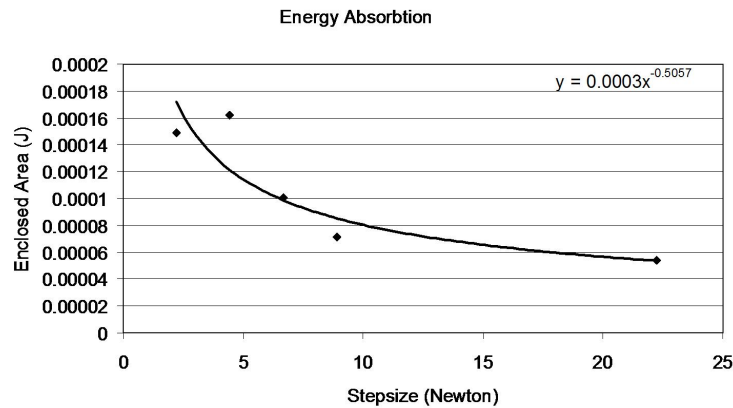


Figure 6.6 Impact of step size variation on the loop areas during static loading

#### 6.2.2.2 LOADING RATE

Loading rate can also greatly affect the area of the hysteresis loop. Fig. 6.7 shows the effects of relaxation in the structure on the load being measured as a function of time. These measurements were conducted on a honeycomb composite structure, shown on the left in Fig. 6.9, with a Nomex core and carbon fiber skin. A crack in the honeycomb core of the structure can be seen on the left in Fig. 6.9, where a manual operated loading frame was used in the experiment.

The structure was loaded to 40 Newtons and then left to relax with current load reading on the force gauge taken every 10 seconds. As shown in Fig. 6.7, the measured load begins to decrease dramatically at first; nonetheless, the rate of change begins to subside the longer the structure has been loaded. It is speculated that this is due to the fibers from the crack meshing and tangling together. The same phenomenon is observed when the structure is being unloaded, although, the curve would be mirrored horizontally.

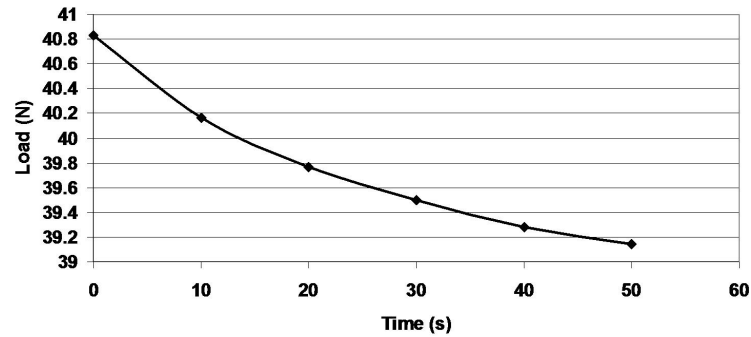


Figure 6.7 Effects of relaxation in the structure on the measured load

### 6.2.3 INITIAL TEST PANEL - CRACK VS BUCKLE

The initial test panels were fabricated in labs at Iowa State University. While the panels were not factory quality, for initial experimentation they proved suitable. The panels are honeycomb composite specimens with a Nomex core roughly an inch thick and a carbon fiber skin with eight to ten plies. A puck, two inches in diameter, is loaded onto the panels until failure using an MTS machine. After loading, the panel was cut into strips one half inch wide, shown in Fig. 6.8, so that the damage to the core could be observed.



Figure 6.8 Test panel cut into strips so that the damage to the honeycomb could be examined



The two panels, shown in Fig. 6.9, were loaded to different values. Panel C1 was loaded to 750 pounds before failure and panel C2 was loaded to 1000 pounds before failure. After close inspection, panel C1 appeared to have more damage to its honeycomb core as compared to panel C2. The damaged region in panel C1 appeared to be a crack, where only a buckle was apparent in panel C2. When the panels were back lit, a very dark region over the flaw appeared in panel C1 and panel C2 remained relatively transparent.

Strips No. 7 and No. 8 on panels C2 and C1 respectively were tested using the manual test setup. A general trend is discovered in these results, as shown in Fig. 6.10. The two damaged panels, panels C1 and C2, produce much larger loop areas than the undamaged panel. Panel C1, the cracked panel, appeared to be more heavily damaged than panel C2 by visual inspection. Although panel C1 had a higher stiffness than C2, its hysteresis loop seemed to show that it would have the most absorbed energy out of the three; however, these curves cannot be compared because they did not reach the same peak load. These results are favorable, showing a favorable correlation between loop area and damage. Also, the force-displacement curve on the panel containing no damage has a much higher stiffness and displays no hysteresis.

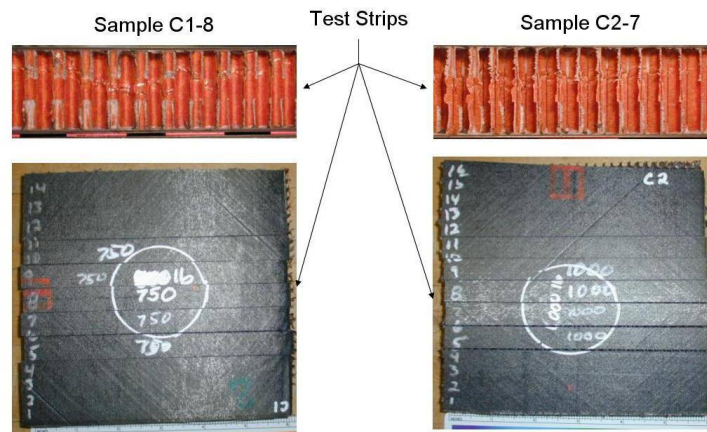


Figure 6.9 Two test strips used for experiments: Panel C1-8(left) containing a crack in the honeycomb core, panel C2-7(right) containing a buckle in the honeycomb core

Skin Thickness:	C1-1.095 mm
	C2-1.143
Honeycomb Height:	25.4 mm
Honeycomb Cell Size:	4.953 mm

Table 6.1 Properties of the test panel shown in Fig. 6.9

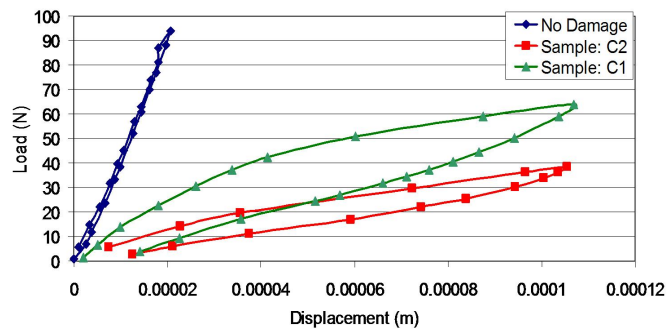


Figure 6.10 Hysteresis loops taken on panels C1 and C2 as well as an undamaged panel

#### 6.2.4 SECOND TEST PANEL - IMPACT DAMAGES

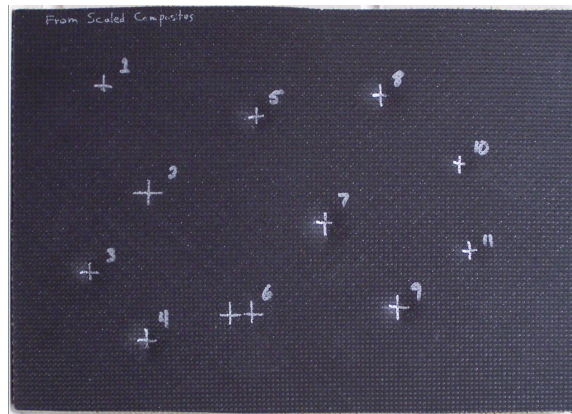


Figure 6.11 Test panel from Scaled Composites

Damage Point	Damage Energy (Joules)	Impactor Diameter (cm)	Impactor Mass (grams)	Drop Height (meters)
1	1.35	3.81	225	0.616
2	0.60	2.54	67	0.914
3	4.04	3.81	225	1.830
4	4.71	3.81	225	2.134
5	2.58	3.81	225	1.169
6	0.67	3.81	225	0.305
7	6.06	3.81	225	2.743
8	3.36	3.81	225	1.522
9	5.38	3.81	225	2.437
10	1.80	2.54	67	2.743
11	2.02	3.81	225	0.914

Table 6.3 Impact energies used to create damages on a thin-skinned honeycomb composite panel from Scaled Composites

Skin Thickness:	0.686 mm
Honeycomb Height:	19.05 mm
Honeycomb Cell Size:	2.54 mm

Table 6.2 Properties of the test panel shown in Fig. 6.11

An industrial grade structure from Scale Composites, shown in Fig. 6.11, was for experimentation. The properties of this structure are shown in table 6.2. Several impact damages were induced on the structure, with each damage marked on the surface of the structure with a number. Table 6.3 lists the properties of each damage.

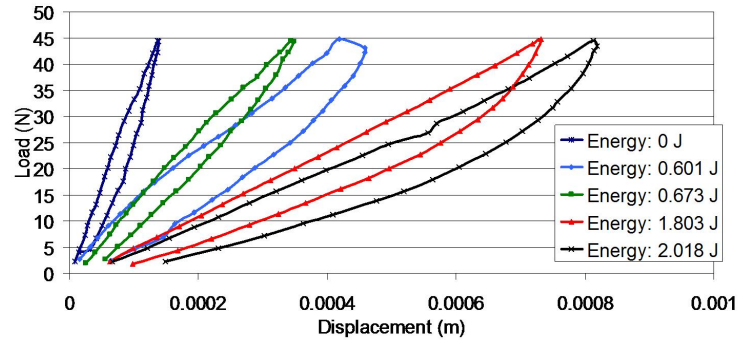


Figure 6.12 Hysteresis loops produced from the Scaled Composites test structure when statically loaded using the manual loading setup

$$P.E. = mgh \quad (6.1)$$

The Scaled Composites structure was not cut into strips after it had been damaged. To measure the level of damage, the amount of energy in the impact was calculated using equation 6.1, where P.E. is potential energy,  $m$  is mass,  $g$  is gravitational acceleration, and  $h$  is the height from which the impactor was dropped. The energy calculated was later used for comparison between flaws. Allowing the structure to stay in one piece provided a more realistic hysteresis loop measurement. Using the manual loading setup, hysteresis loops were generated while loading the Scaled Composites structure, as shown in Fig. 6.12. Fig. 6.12 and Fig. 6.13 represent positive correlation between loop area and impact energy. The stiffness of the impacted regions also seems to correlate well with impact energy, i.e., the greater the impact energy, the lower the stiffness after the impact.

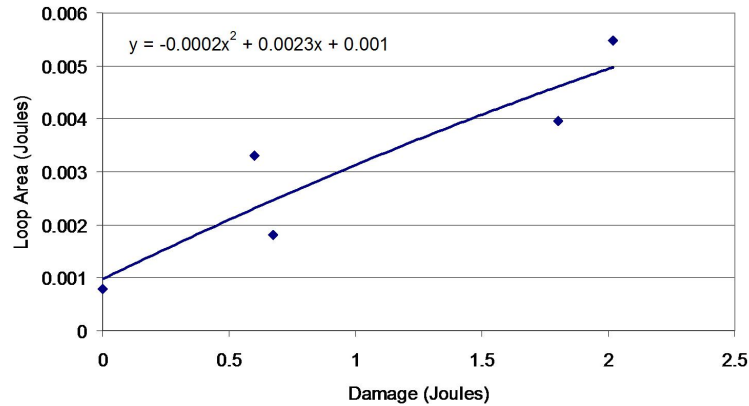


Figure 6.13 Energy absorbed by the Scaled Composites test panel derived from the corresponding hysteresis loops

#### 6.2.4.1 INSTRON TESTING

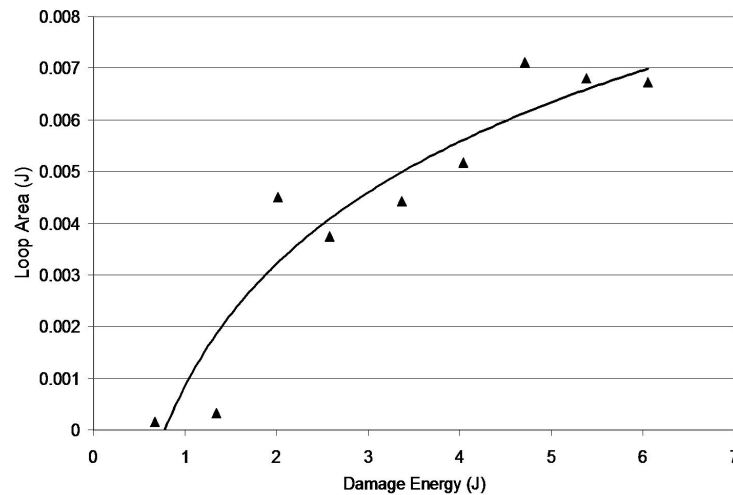


Figure 6.14 Absorbed energy curve on Scaled Composites panel using INSTRON machine

Similar to an MTS machine, the INSTRON machine allows for accurate control of step size and loading rate. The results of an experiment conducted on the Scaled Composites specimen

are shown in Fig. 6.14. Again, the results are quite favorable, showing an increase in loop area with increasing damage energy.

Relative loop areas between the data taken using the manual test setup versus the INSTRON setup are similar over the regions the data overlaps; although, the manual test data had a higher loop area, on average, than the INSTRON setup. It is probable that this is due to the fact that the INSTRON machine had a slower loading rate ( $0.003 \frac{mm}{sec}$ ), allowing the panel to more fully relax to relieve some stress. In result, this lead to a longer loading duration on the sampling, allowing for total loaded times of up to 26 minutes. Loading durations using the manual loading setup were on average less than 20 minutes.

### 6.3 DYNAMIC LOADING

The method of dynamic loading can also be used to generate a stress-strain curve. Dynamic loading allows the structure no time to relax and relieve the stress; loading curves are generated nearly instantaneously, having total loading times of the order of one millisecond. Although, because dynamic loading allows no relaxation time, the issue of the stress-strain curve no longer showing a hysteresis effect becomes a concern. As shown previously, loading rate and step size variation strongly affect the size of the hysteresis loop. Yet, as the loading rate becomes faster, the relative effect on the hysteresis loop decreases. If the curve in Fig. 6.6 is interpolated to infinity, or very fast loading rates, it should show that loop areas produced over the same region become constant as a function of loading rate. In spite of this observation, the dependence upon loading rate must still be experimentally investigated.

When moving from static loading to dynamic loading, a one sided method is sought because a two sided method for in-the-field inspection is not possible. Access to one side of the part is available in nearly every inspection situation. Load is relatively simple to measure with one sided access; however, displacement proved to be a great challenge and the majority of the research performed was devoted to this topic. A possible solution, using suction cups to attach the loading apparatus to the outer surface of the structure, presents a large concern because of the uncontrolled movement of the individual suction cups. The testing apparatus would also

be large and cumbersome; therefore, this approach was not pursued.

The second method considered makes use of an accelerometer similar to that of the CATT system. When tapped on the surface of the structure, the accelerometer measures acceleration as a function of time. Theoretically, this curve could be integrated twice to produce a displacement curve. The load (i.e. force) could also be obtained using the instantaneous values of acceleration based on  $F = ma$ , where  $m$  is the known mass of the accelerometer. The method also remains one sided and provides a very quick method of obtaining a stress-strain curve. This method has the potential for being a viable technique of obtaining a hysteresis loop by simply tapping the surface of the structure.

### 6.3.1 DEDUCTION OF FORCE-DISPLACEMENT CURVES FROM ACCELERATION

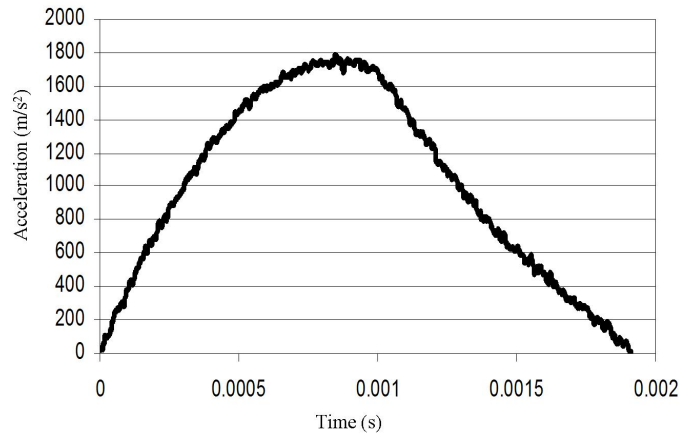


Figure 6.15 Typical acceleration curve produced from a tap

Calculus explains that acceleration can be integrated to provide velocity, and velocity, in turn, can be integrated to provide displacement. The initial conditions at each integration, for example, initial velocity and initial displacement, must be known to solve for correct values of displacement and velocity. The results obtained from integrating acceleration are shown in equations 6.2-6.4, where  $V_0$  and  $D_0$  are the constants of integration.

$$A(t) = f(t) \quad (6.2)$$

$$V(t) = \int A(t)dt + V_0 \quad (6.3)$$

$$D(t) = \int \int A(t)dt dt + V_0 t + D_0 \quad (6.4)$$

### 6.3.1.1 DISCRETE INTEGRATION

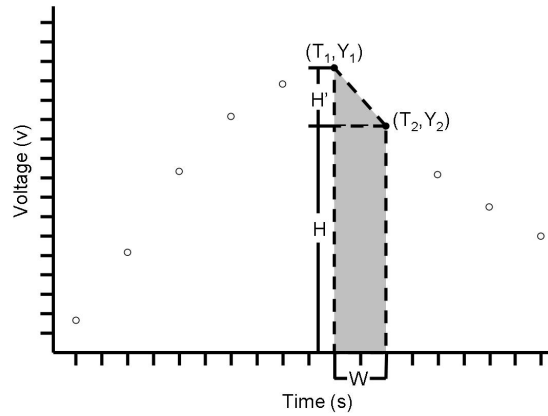


Figure 6.16 Area under the curve between two adjacent points using discrete data

The data received by an oscilloscope from the accelerometer is discrete; it comes in the form of a list of data points which can be plotted to form a curve. In order to integrate these curves, a discrete integration technique must be used, in which the area beneath adjacent data points will be calculated and summed to produce the total area under the curve. This process is shown in Fig. 6.16, where the area between two adjacent points is calculated. Equation 6.5 provides the formula for calculating the area enclosed by a trapezoid, where the Y and T are the values of the data points represented on the two axis. The discrete data points are then stepped through, calculating the area below the two current points and summing them together. The total sum of all the points provides the value of the integral. Equation 6.6 presents the formula of total area for a data set consisting of n points, where  $A_t$  is the total area and  $A_i$  is the area below two adjacent data points.



$$A_i = \left( \frac{Y_1 + Y_2}{2} \right) (T_2 - T_1) \quad (6.5)$$

$$A_t = \sum_{i=1}^n A_i \quad (6.6)$$

Referring back to equations 6.2-6.4, initial values are required to solve for velocity and displacement. The positive direction of acceleration will be defined as being normal to the structure surface and zero displacement will be defined as the undisturbed structure surface. The initial value of displacement,  $D_0$ , is zero because the acceleration curve begins when the accelerometer first makes contact with the structure surface. This leaves only the initial velocity,  $V_0$ , to be solved, for which one boundary condition is needed.

There are three different methods for which the initial velocity can be determined. Initial velocity is simply the impact velocity of the tapper; therefor, the first method is simply controlling impact velocity using the testing apparatus. This method will be called “direct measurement” for the remainder of this thesis. The second method sets the inflection point of the velocity curve to zero and will be called “Inflection Point Method”. The inflection point represents a change in the direction of velocity at which the velocity must cross the zero axis. Setting this point to zero will determine the initial velocity. An inflection point is found by referencing the acceleration curve; this point occurs at the same time the acceleration reaches its peak. Equation 6.7 provides the boundary condition equations for this method. Selection of a valid peak acceleration can become difficult because of the noise in the signal and shows a level of uncertainty when using this technique.

$$\begin{aligned} A(t) &= \max @ t = t_1 \\ V(t_1) &= 0 \end{aligned} \quad (6.7)$$

Finally, the third method makes an assumption that the structure is fully returned to its original state when the acceleration crosses the zero axis the second time. This point in time corresponds to the point at which the accelerometer is no longer in contact with the surface

of the structure. If the structure is fully elastic, this point would also mean that the structure surface has returned to its original shape. The displacement at this point is set to zero as shown in equation 6.8. It is an iterative method, where the initial velocity is continually adjusted until the selected point on the displacement curves becomes zero. The Inflection Point Method is used as an initial guess for initial velocity; the method then iterates from there. This method for calculating initial velocity is questionable and also has some uncertainty to it because it is not proven that the structure is able to fully return to its original state during this very short time frame. This method will be called “Zero Acceleration Method” for the remainder of the thesis.

$$A(t) = 0 @ t = t_2 \text{ where } t_2 \neq 0$$

$$D(t_2) = 0 \tag{6.8}$$

### 6.3.1.2 EFFECTS OF HYSTERESIS

The acceleration curve is generally a bell shaped curve, although it is usually asymmetric. Fig. 6.15 shows a feature observed in the acceleration curve when produced from a tap over a heavily damaged region. The curve is slightly asymmetric, with the right half representing an under damped system with a long settling time. More specifically, after the acceleration has reached a max value, the instantaneous values of acceleration can have an exponential decay. The quality is often very subtle, almost unnoticeable to the naked eye; nevertheless, it is believed to be one factor that contributes to the development of the hysteresis loops seen in the stress-strain curves.

This hysteresis effect can be shown using theoretical values as represented in Fig. 6.17. The acceleration curve is approximated by the half cycle of a sine wave where it is symmetric about a vertical line through its peak. The curve was integrated once to produce the velocity curve and then again to produce the displacement curve while using the inflection point method to approximate the initial conditions. The force-displacement curve, equivalent to the stress-strain curve, is shown on the bottom of the figure. The hysteresis effect is absent and the

loading and unloading curves follow a straight line, which is representative of an undamaged region.

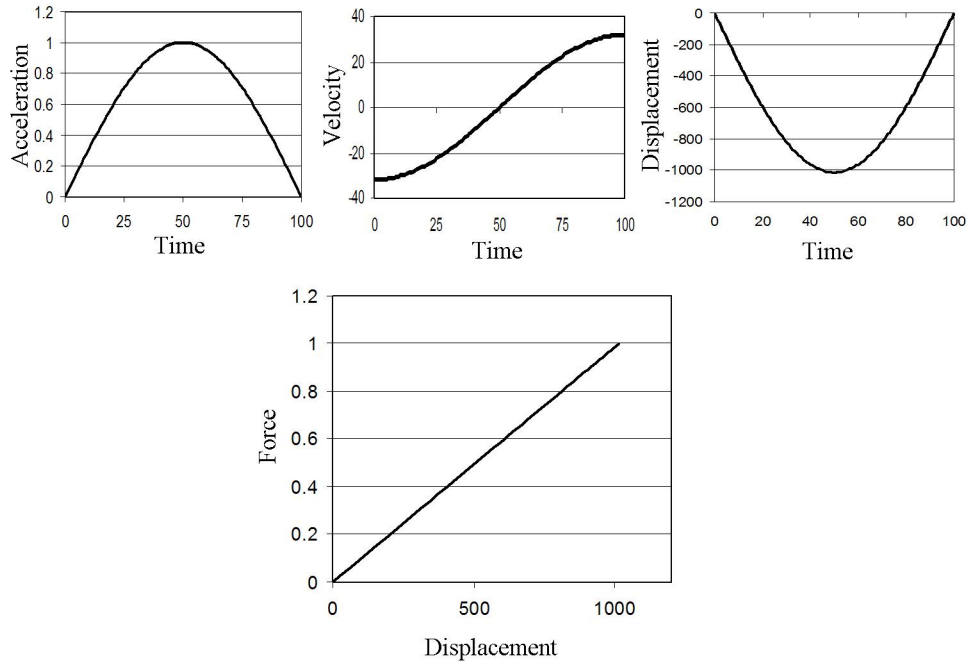


Figure 6.17 Theoretical acceleration, velocity and displacement curves as well as a hysteresis loop calculated from an acceleration curve approximated by a bell curve. For simplicity the displacement was plotted as the negative of its calculated value

The acceleration curve of a damaged region is modeled in Fig. 6.18. The proportions of this acceleration curve are exaggerated in respect to an experimental acceleration curve, shown in Fig. 6.15, so that the effects can be easily observed. The curve is approximated by a quarter cycle of a sine wave from the origin to the peak. After the curve has reached its peak value, the curve is then approximated by an exponentially decaying function for the second half of the curve. It is only theorized that the acceleration curves would take this shape over a damaged region. Often times, in experimental results, the effects in the acceleration curve are very subtle and prove to be difficult to observe. However, it is believed by this author that this

effect is one of the sole causes of the hysteresis effects shown in the force-displacement curves.

This curve is integrated to give velocity, displacement and the resulting force-displacement curve. As shown in Fig. 6.18, the force-displacement curve shows a hysteresis loop. Effects of this exponential decay are also displayed in the velocity and displacement curves. The velocity curve is shifted downwards, conveying a quicker incident velocity than rebound velocity. This property also seems to be a variable dependent upon energy absorption within the structure and could be considered as another flaw detection method. The displacement curve becomes asymmetric, having a longer fall time than rise time.

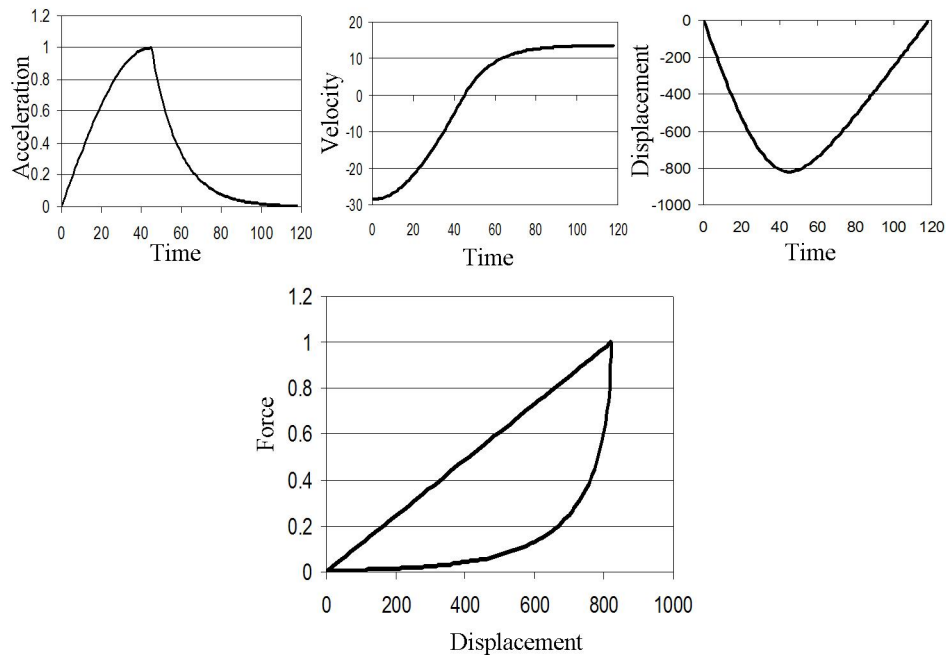


Figure 6.18 Theoretical acceleration, velocity and displacement curves as well as a hysteresis loop calculated from an asymmetric acceleration curve. For simplicity the displacement was plotted as the negative of its calculated value

It can be concluded from these theoretical experiments that the two factors in the acceleration curves which lead to the development of hysteresis loops are asymmetry and a slight

exponential decay on the second portion of the curve. If these two factors are not present, the resulting force-displacement curve will be a straight line having no hysteresis. The force-displacement curve produced in Fig. 6.18 used an acceleration curve containing both of these features and bears a striking resemblance to experimentally obtained hysteresis loops. While the asymmetry is very prevalent in experimentally obtained acceleration curves, the exponential decay is a much harder feature to notice. It is hard to say if the exponential decay is present in all experimentally obtained acceleration curves; however, it was the only to theoretically produce hysteresis loops similar to those obtained when the structure was statically loaded.

### 6.3.2 EXPERIMENTAL VERIFICATION

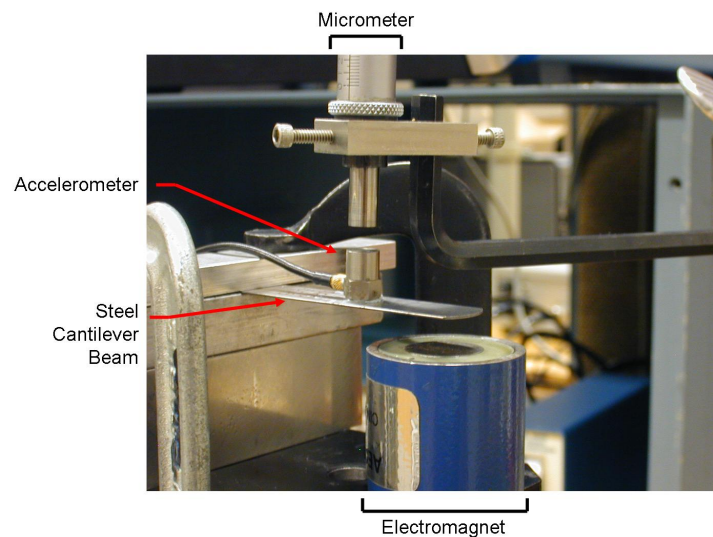


Figure 6.19 Experimental setup used to measure total displacement of an accelerometer attached to a cantilever beam

Theoretical results proved promising; however, they must be supported by experimental results. Fig. 6.19 shows the experimental setup used to verify the accuracy of the acceleration integration technique. Displayed in the image is an accelerometer, the cantilever beam it is attached to, an electromagnet used to release the beam, and the micrometer used to measure the total distance traveled by the accelerometer.

The accelerometer is mounted to the cantilever beam using wax, which is known to be one of the best methods for attachment because it has very little effect on the measured acceleration. The electromagnet is then turned on and the cantilever beam is bent down so that it is held in place by the electromagnet, displayed in Fig. 6.20. The micrometer is used to measure the distance to the top surface of the accelerometer, which will later be used as the constant of integration  $D_0$ . After measurement of the loaded position, the micrometer is moved up so that it will not be hit when the beam is released. The cantilever beam is released and reloaded several times while the micrometer is iteratively adjusted so that the top surface of the accelerometer just makes contact with its anvil on the upswing. This measurement,  $D$ , is representative of the maximum height the accelerometer achieves. Finally the beam is allowed to go to equilibrium, where the equilibrium position is defined as zero.

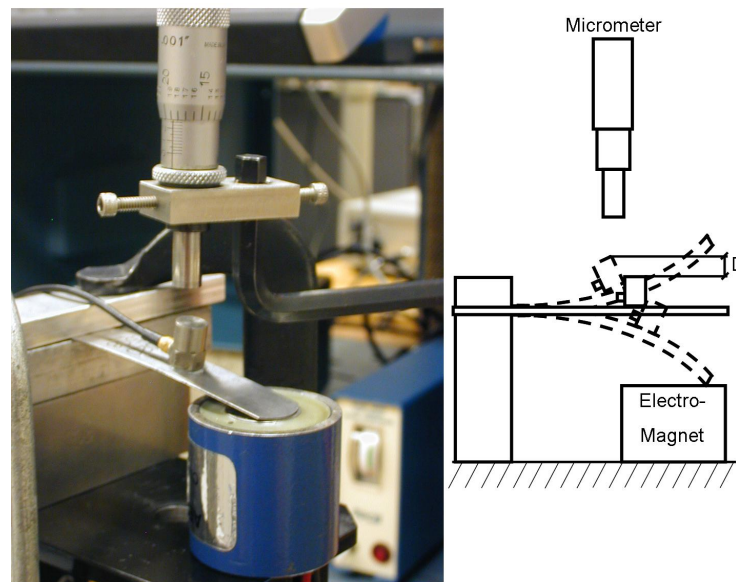


Figure 6.20 Cantilever beam being held by the electromagnet

During this process, distance measurements were taken in order to produce  $D$ ; the output voltage from the accelerometer was also captured. The accelerometer output can be integrated to produce the displacements and their values are checked against the measured values. The boundary conditions, however, have changed from that of a normal tap. Now the accelerometer

is starting at rest,  $V_0 = 0$ , and has an initial negative displacement,  $D_0$ .  $D_0$  was measured during the experiment with the micrometer.

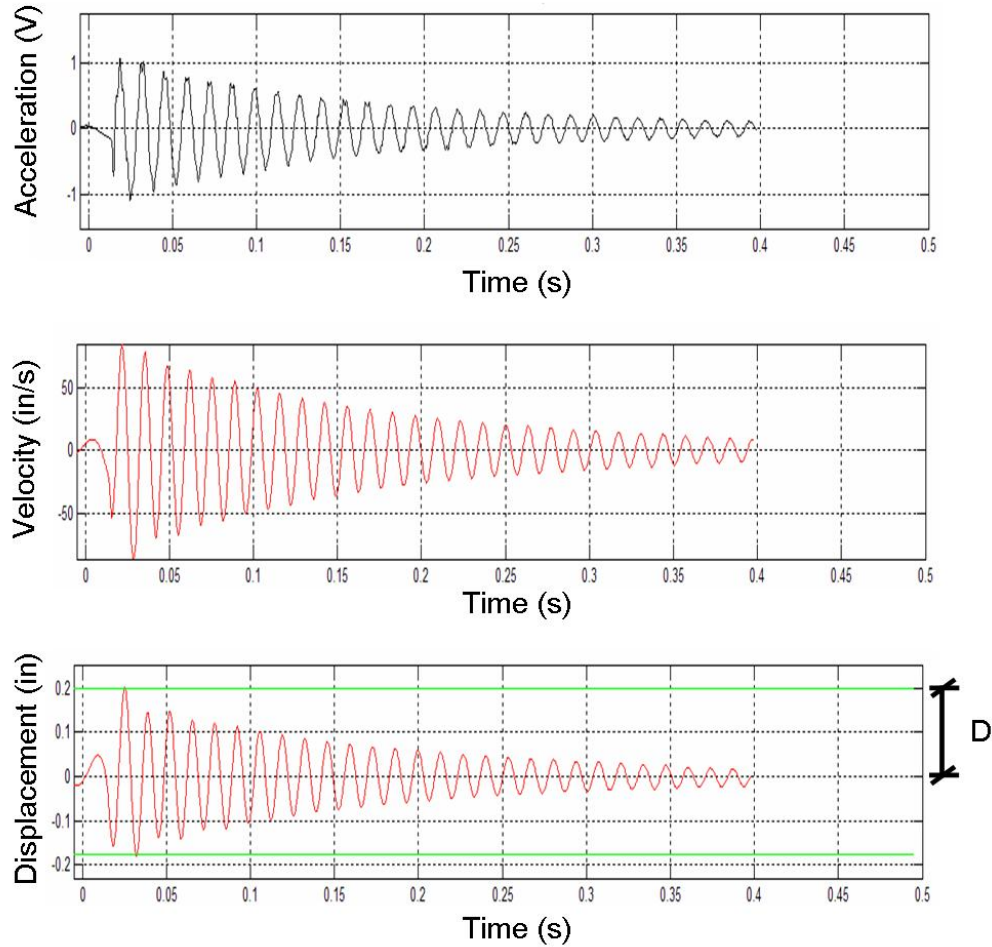


Figure 6.21 (Top) Voltage output from the accelerometer, (Middle) Velocity integrated from acceleration with  $V_0 = 0$ , (Bottom) Displacement integrated from velocity with an initial condition of  $D_0$

Fig. 6.21 illustrates the results of the integration of acceleration. The original accelerometer signal is shown on the top with the integrated velocity and displacement curves below it. The

curve of interest is the displacement, where  $D$  can be read from the displacement curve and compared to the measured values. The top green line on the displacement graph shows the calculated  $D$  value obtained using the acceleration integration technique. Fig. 6.22 displays the results of this experiment where the data are plotted as measured versus calculated  $D$  value, which would show a perfect correlation as a 45 degree line. As displayed on the graph, the data correlate well with all points around a 45 degree line. These experimental results verify theoretical conclusions that a discrete integration technique can be used on the output of an accelerometer to compute velocity and displacement.

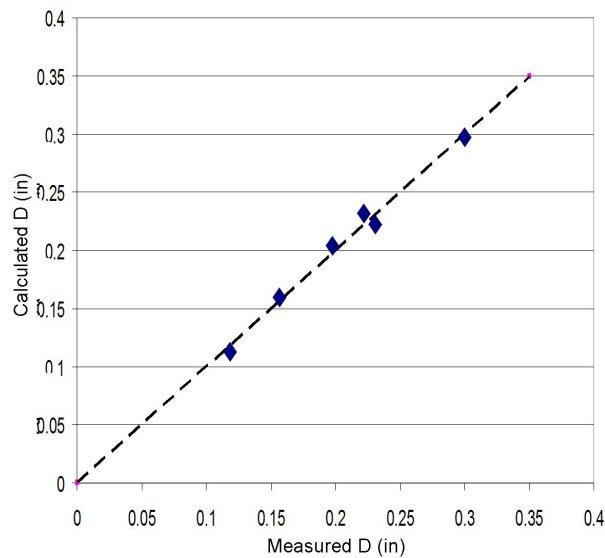


Figure 6.22 Correlation between calculated distance using the accelerometer output and the measured distance

### 6.3.3 STATIC VERSUS DYNAMIC LOADING

The Scaled Composites test panel, displayed in Fig. 6.11, was used to evaluate the static loading and dynamic loading against each other. Hysteresis loops were calculated for each point on this structure using dynamic loading. The accelerometer was dropped from 10.16 cm above the structure surface, where the acceleration signal for the first impact was captured. The data were plagued by a low signal-to-noise ratio, so a 20 point running average technique



was used to smooth the data before integration.

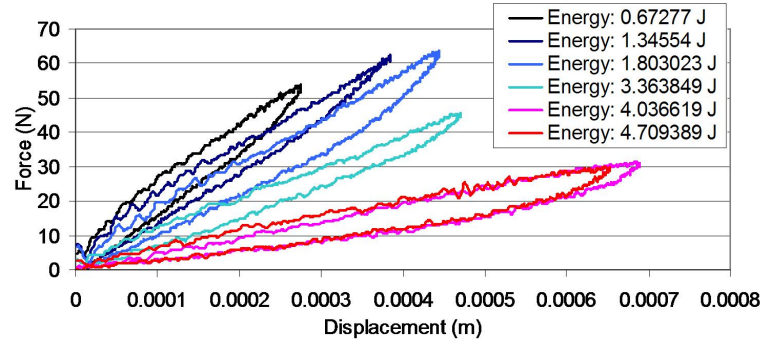


Figure 6.23 Hysteresis loops taken on the Scaled Composites panel using dynamic loading

During the first integration attempt, the Inflection Point Method was used to solve for the initial value; yet, this method lead to hysteresis loops having loading curves below unloading curves. This phenomenon is theoretically impossible and equates to energy being added, not absorbed, during the course of the impact. This method is very sensitive to the selection of the inflection point on the velocity curve. It is believed that the low signal-to-noise ratio increased the uncertainty of this process which makes it very difficult to use. Therefore the Zero Acceleration Method was used to solve for these initial value.

When using this method, the results were favorable and the method appears to be much more stable. As illustrated in Fig. 6.23, the loop area as well as the slope of the curve appear to correlate well with damage. That is, the loop area increases and the average slope of the load and unload curves decrease as the impact energy that causes the damage increases. Comparisons between dynamic loading and static loading are shown in Fig. 6.24 and Fig. 6.25, where the hysteresis loops, obtained both statically and dynamically over the same point on the sample, are plotted.

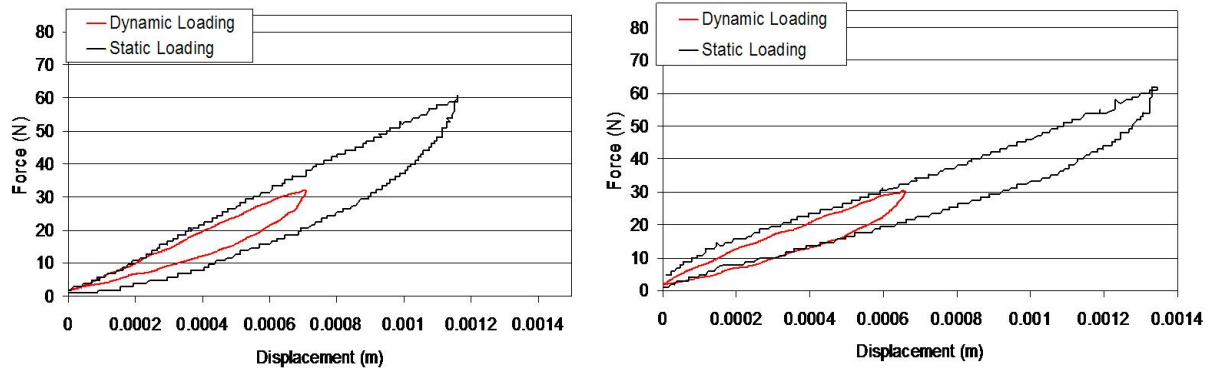


Figure 6.24 Comparison between static and dynamic loading: (Left) loops taken over an impact damage of 4.04J on the Scaled Composites panel, (Right) loops taken over an impact damage of 4.71J on the Scaled Composites panel

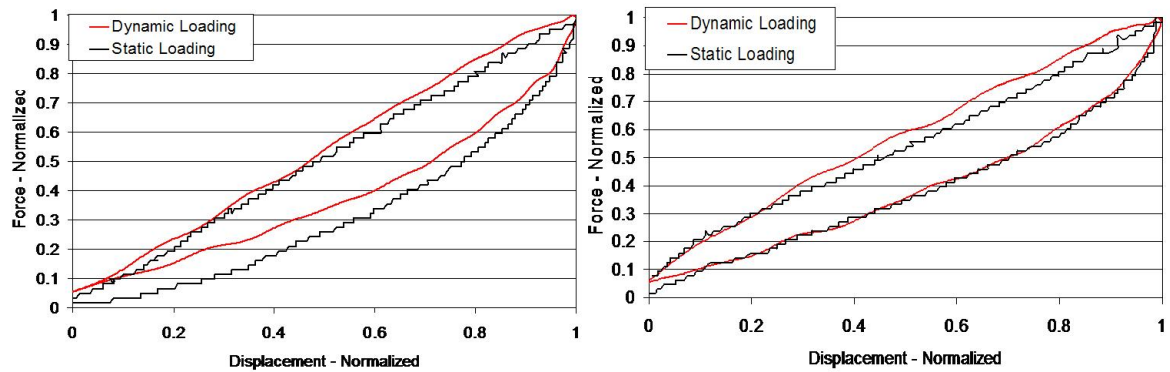


Figure 6.25 Comparison between static and dynamic loading where both load and displacement have been normalized to one: (Left) loops taken over an impact damage of 4.04J on the Scaled Composites panel, (Right) loops taken over an impact damage of 4.71J on the Scaled Composites panel

Fig. 6.24 plots the loops without any normalization. Although the dynamic loading did not load the structure as heavily, the general shape and slope of the two curves are surprisingly similar for each graph. Fig. 6.25 plots the curves having normalized displacement and load in order to compare the shapes of the curves. Again, the two curves on each graph are very similar. These results are favorable due to the fact that there is such a large difference in test duration between static versus dynamic loading and this difference appears to have no effect; the curves are nearly identical. One question to be posed is whether or not these curves should agree. During static loading, the structure has much more time to relax. As a result, the hysteresis loops will grow larger. This effect was observed when the step size variation was being studied.

#### 6.3.4 STIFFNESS CORRELATION

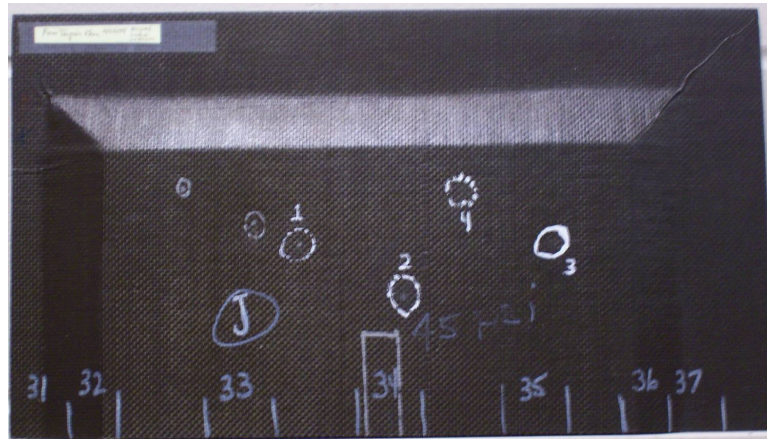


Figure 6.26 Test panel used for stiffness correlation

Skin Thickness:	1.372 mm
Honeycomb Height:	10.80 mm
Honeycomb Cell Size:	2.87 mm

Table 6.4 Properties of the test panel shown in Fig. 6.26

Chapter 4 discussed how to compute local stiffness from the contact time of a tap, using equation 5.7, which proved to be a very useful approximation. Stiffness can also be directly measured from the stress-strain curve, where the slope of the curve is the stiffness. A second method of verifying the accuracy of the hysteresis loops would be to compare the two stiffness values. A new test panel was adopted for this study, shown in Fig. 6.26.

This new panel is composed of a Nomex honeycomb core roughly one half inch thick with the face sheets having a carbon/epoxy layup, the properties of which are shown in table 6.4. The structure was tapped by hand over nearly its entire surface, including damaged and undamaged regions, in the same process a tap test would be conducted; although, rather than solely capturing the contact time,  $\tau$ , the entire waveform was captured. The stiffness was computed from the  $\tau$  with equation 5.7. The acceleration signal was integrated to produce velocity and displacement; ultimately allowing the force displacement curve to be plotted. Originally, Zero Acceleration Method was used to solve for the initial conditions. This method began to produce an unloading curve which was higher than the loading curve, as was seen previously with the Inflection Point Method. A new method for solving for these initial conditions was needed.

The tap signal received was slightly different than the previous tests performed where the accelerometer was dropped from a set distance. Now the accelerometer was being held by hand and tapped on the surface of the structure. Fig. 6.27 shows the difference in the expected signal and the actual signal observed, where the acceleration dips below the baseline briefly on its trailing edge. A negative acceleration represents a force acting on the accelerometer, which would be forcing the accelerometer back into the structure after it has rebounded. The force of gravity is obviously contributing to this result, yet the magnitude of this negative acceleration would require a force much larger than gravity.

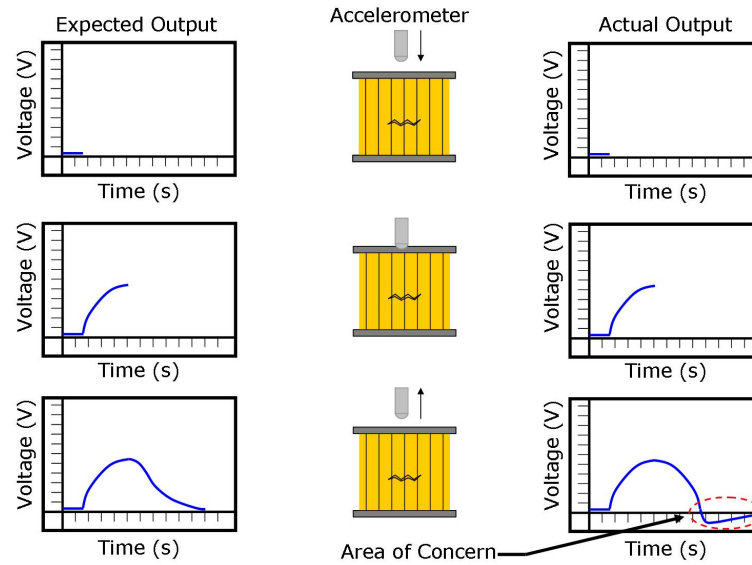


Figure 6.27 Expected accelerometer output versus actual accelerometer output showing the drop below the baseline

The cause of the negative acceleration was found to be the gripping force on the accelerometer applied by the tester while performing a hand tap. As the force of the grip on the accelerometer increases, the acceleration curve dives further into the negative region. Fig. 6.28 shows the effects of this gripping force. There are three curves displayed in the figure, each of which were generated over the same region of the structure and was intentionally made to reach the same peak. The lightest curve corresponds to the accelerometer being simply dropped onto the structure, without any gripping force added to the accelerometer. This curve appears to return to the baseline without any undershoot. The second curve, corresponding to a light grip, dives below the baseline. This curve has some undershoot on its trailing edge. Finally, the bottom curve was generated by very tightly gripping the accelerometer while tapping. This curve has a larger undershoot than the other two and dives well below the baseline. Using an accelerometer with a calibration of  $10 \frac{mV}{g}$ , the signal reaches nearly 0.5 volts below the baseline. Corresponding to an acceleration value of  $490 \frac{m}{s^2}$ , it is nearly 50 times the value of gravitational acceleration. Interestingly, prior to the acceleration curve crossing the baseline, the effect of gripping force has no effect, according to Fig. 6.28. The curves are nearly identical

prior to the crossing of the baseline.

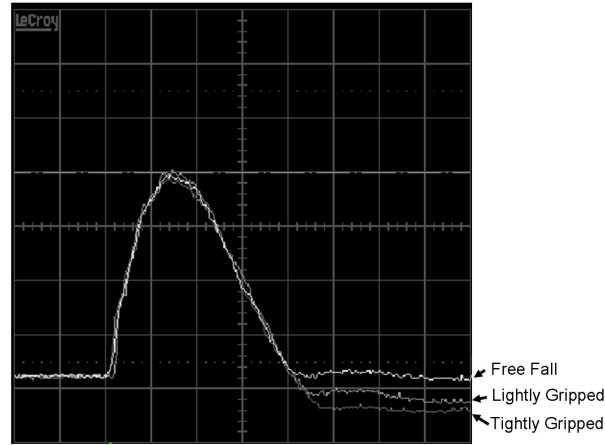


Figure 6.28 Effect of the gripping force on the accelerometer when used in a hand tap. Time Scale: 0.1ms per division, Voltage Scale: 1.00V per division

The Zero Acceleration Method of the initial value solutions sets displacement equal to zero where the descending acceleration curve crossed the zero axis. When the accelerometer was dropped, this point corresponded to the lowest point on the acceleration curve; however, when the accelerometer is gripped, it is no longer the lowest point. The new technique for solving initial value made use of the minimum acceleration, setting this point on the displacement curve equal to zero. Shown in equation 6.9, this initial condition appeared to work well for the remainder of the experiments conducted. This method for solving initial conditions will be known as “Minimum Acceleration Method”.

$$A(t) = \text{minimum} @ t = t_3 \text{ where } t_3 \neq 0$$

$$D(t_3) = 0 \quad (6.9)$$

Using the initial condition displayed in equation 6.9, the acceleration curve was able to be integrated successfully and a feasible force-displacement curve was obtained. Stiffness was calculated from the force-displacement curve by calculating the slope to each individual point

on the curve, and subsequently, taking the average of all the slopes to give an average slope for the entire curve. The two values were then plotted against each other in Fig. 6.29. A 45 degree line would again represent a perfect correlation between the two values.

The results displayed in Fig. 6.29 are favorable. Although the data does not form a perfect 45 degree line, it is very close. The amazing property of this curve is the tight grouping of the data, where data points have very little spread to them. Given the amount of data collected, this is remarkable and is yet another verification of the validity of the acceleration integration method and its corresponding force-displacement curve.

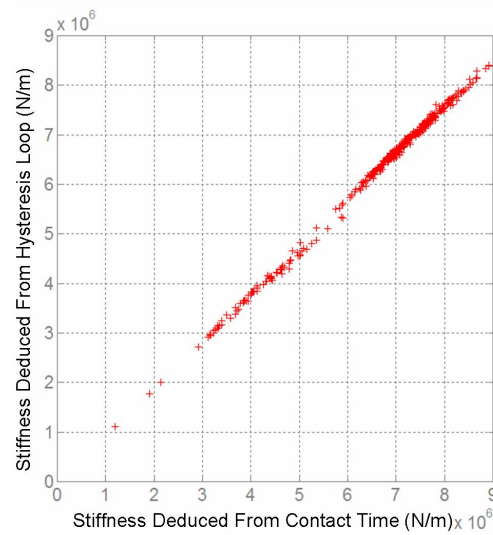


Figure 6.29 Correlation between the stiffness computed from tau and the stiffness computed from the force-displacement curve. The data points were collected over a 17x25 grid (425 data points)

### 6.3.5 BELL TEST PANELS

Bell Helicopter provided three honeycomb test panels, displayed in Fig. 6.30, Fig. 6.31, and Fig. 6.32, all having Nomex honeycomb cores. Only panel B has carbon/epoxy face sheets, while the other two had fiberglass/epoxy face sheets. The three panels were damaged with a 1.5 inch diameter steel ball dropped from various heights. The method for calculating damage

was very similar to that used with the Scaled Composites panel; however, the rebound height was taken into account as a means of producing more accurate damage data.

The ball bearing was elevated to a designated height and then released with zero velocity. The steel ball was allowed to impact the structure once and rebound. After the ball bearing reaches the peak height of its rebound, it was caught on its decent. The entire process was digitally recorded so the peak rebound height could be observed. The potential energy associated with the maximum rebound height was subtracted from the potential energy of the drop height to produce total absorbed energy by the structure, assuming the energy absorbed by the structure is the only cause of the change in potential energy. This is outlined in equation 6.10, where  $m$  is the mass of the tapper,  $g$  is the gravitational acceleration,  $h$  is the drop height, and  $h_{rebound}$  is the rebound height of the ball bearing.

$$\text{Absorbed Energy} = mg(h - h_{rebound}) \quad (6.10)$$

Only panels A and B were damaged after receiving the set of panels; panel C already contained embedded flaws. Tables 6.6 and 6.8 display the information of each damage induced on the panels. The number associated with each damage is marked on the surface of the panel. To represent a skin-to-core disbond or a fracture in the honeycomb, panel A was also damaged on the left edge using a putty knife . The dimensions and the depth of the cut are marked on the surface of the panel.



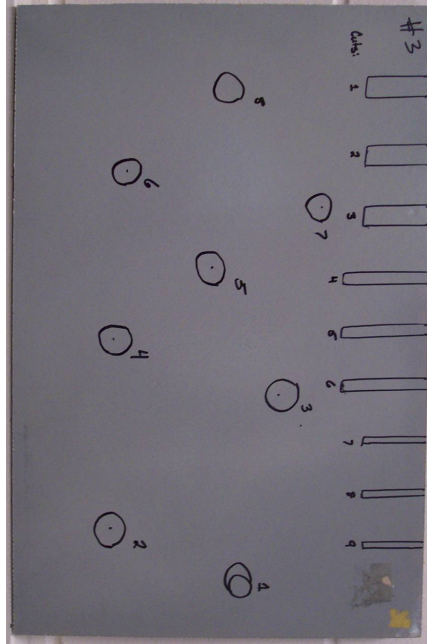


Figure 6.30 Bell Helicopter test panel A

Skin Thickness:	0.991 mm
Honeycomb Height:	17.35 mm
Honeycomb Cell Size:	8.97 mm

Table 6.5 Properties of the test panel shown in Fig. 6.30. Honeycomb cell size refers to the distance between two parallel walls

Throughout the course of studies performed on these structures, an additional parameter was considered as a possible damage indicator. This parameter was the total change in velocity of the accelerometer through the duration of the tap, more specifically it is the difference between the initial velocity and the final velocity of the accelerometer. This measurement is not sensitive to initial velocity because it measures the relative change in velocity from the point of impact. Even with an incorrect initial velocity selection, the relative change in velocity remains the same. Much of the uncertainty associated with the process of selecting initial velocity is eliminated with this method, making the process very favorable for experimentation.

Damage Site	Damage Energy (Joules)	Impactor Mass (grams)	Drop Height (meters)	Rebound Height (meters)
1	1.20	225	0.826	0.286
2	1.41	225	0.908	0.273
3	1.39	225	0.978	0.353
4	1.46	225	1.073	0.419
5	1.48	225	1.175	0.508
6	1.84	225	1.283	0.455
7	1.81	225	1.391	0.578
8	2.06	225	1.549	0.622

Table 6.6 Impact energies of damages on Bell Helicopter panel A

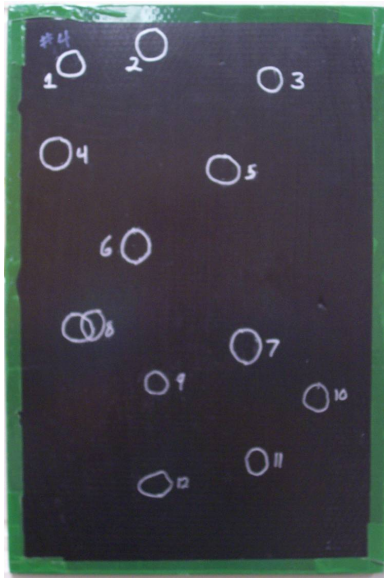


Figure 6.31 Bell Helicopter test panel B

Skin Thickness:	1.016 mm
Honeycomb Height:	22.76 mm
Honeycomb Cell Size:	4.72 mm

Table 6.7 Properties of the test panel shown in Fig. 6.31. Honeycomb cell size refers do the distance between two parallel walls

Damage Site	Damage Energy (Joules)	Impactor Mass (grams)	Drop Height (meters)	Rebound Height (meters)
1	0.78	225	0.559	0.210
2	1.06	225	0.686	0.210
3	1.30	225	0.889	0.307
4	1.64	225	1.086	0.349
5	1.87	225	1.245	0.406
6	2.29	225	1.505	0.476
7	2.40	225	1.562	0.485
8	2.04	225	1.354	0.438
9	1.82	225	1.149	0.333
10	1.49	225	0.978	0.307
11	1.22	225	0.829	0.282
12	0.88	225	0.629	0.235

Table 6.8 Impact energies of damages on Bell Helicopter panel B

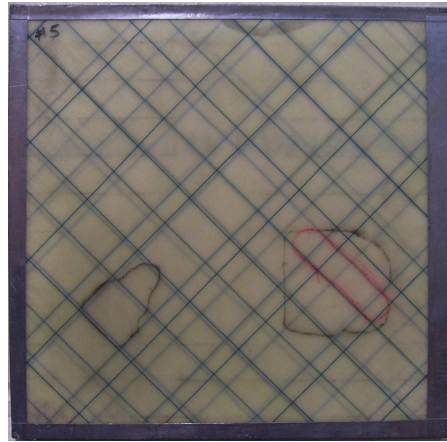


Figure 6.32 Bell Helicopter test panel C

Skin Thickness:	2.210 mm (Top) 1.016 mm (Bottom)
Honeycomb Height:	16.60 mm
Honeycomb Cell Size:	3.00 mm

Table 6.9 Properties of the test panel shown in Fig. 6.32. Honeycomb cell size refers to the distance between two parallel walls

The three panels were tapped at nearly every point on the surface of the sample, where the entire acceleration waveform was captured for each point to allow for the calculation of enclosed area, change in velocity, and  $\tau$  for each point. Contour plots of enclosed area and change in velocity were generated for each panel using a contour plot of  $\tau$  for comparison to a proven method. Of the three methods, no single method prevailed throughout all tests. Each method seemed to have advantages and disadvantages depending upon the panel being tested. The results are shown in Fig. 6.33, Fig. 6.34, and Fig. 6.35.

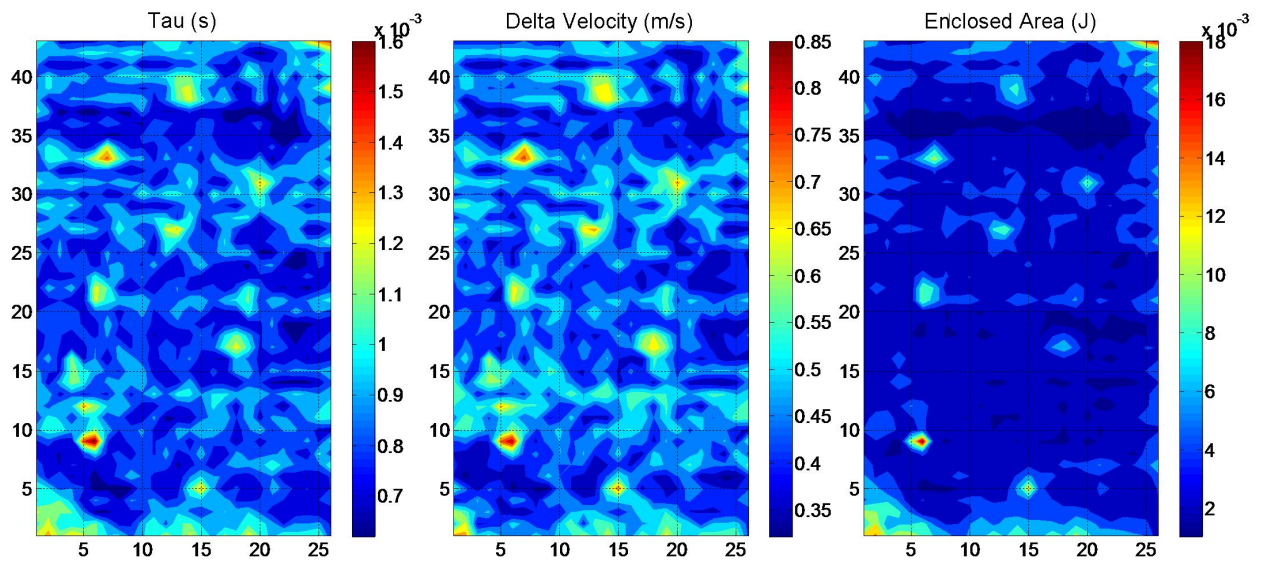


Figure 6.33 Contour images taken from Bell Helicopter panel A

Panel A is composed of fiberglass face sheets enclosing a Nomex honeycomb core, the individual cells contained walls having a five millimeter length and a height of two centimeters. The structure was damaged with impacts in addition to knife cuts along one edge of the panel. Though unexpected, the knife cuts did not have a pronounced representation on any of the resulting images, shown in Fig. 6.33, remaining hidden in comparison to the impact damages. Nearly every impact damage was clearly visible in each image. In this particular experiment, however, enclosed area stands apart from the others; the enclosed area plot displays a very uniform baseline unlike the others. This effect is caused by large honeycomb cells, where the

local stiffness can change greatly depending upon where the tap occurs in relation to the current honeycomb cell it is positioned over. As shown in both the  $\tau$  and delta velocity plots, this effect causes many high and low regions which do not correspond to any damages; however, they may correlate with the honeycomb cells. In this case, the flaws seem to remain visible to the naked eye, yet this nonuniform baseline effect can mask flaws making them very difficult to detect. Enclosed area seems to be relatively unaffected by larger honeycomb cells.

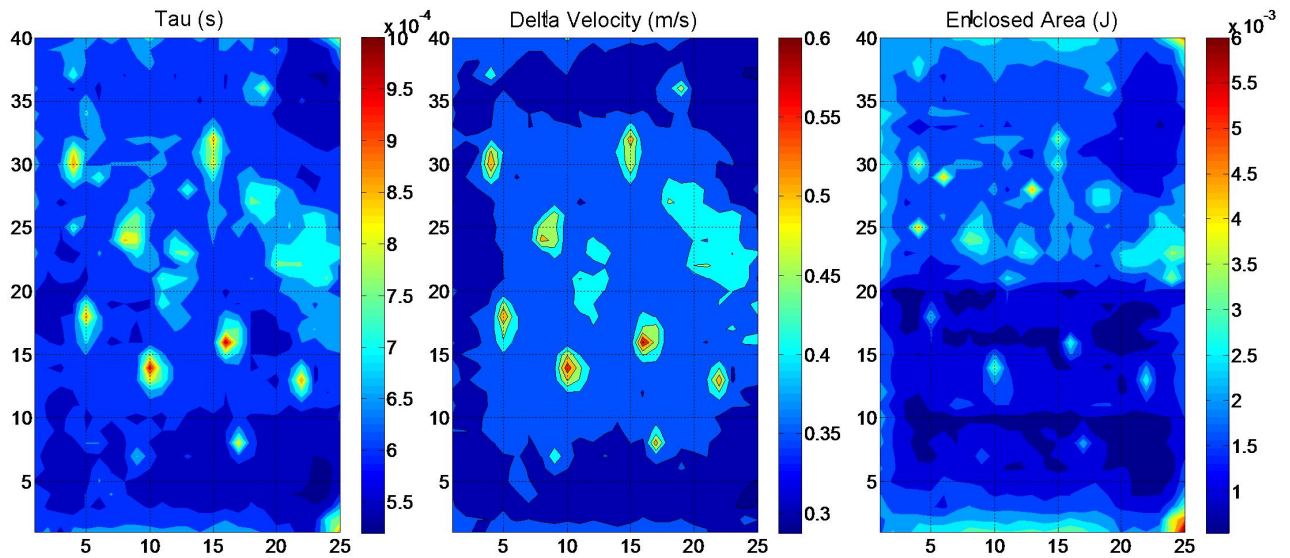


Figure 6.34 Contour images taken from Bell Helicopter panel B

The results produced from panel B, shown in Fig. 6.34, show a different effect compared to the results produced by panel A. This panel is composed of a carbon/epoxy face sheet with a Nomex honeycomb core. The cell size of the honeycomb in panel B is smaller than that of panel A, containing cells with nearly half the size of the cells in panel A. However, the height of the cells was larger, nearly 2.75 centimeters tall. In this case, the  $\tau$  and delta velocity contour plots displayed a uniform baseline in which the flaws were very clearly drawn out. The enclosed area plot had difficulty displaying all flaws on this panel and also displayed the bottom portion of the panel to be darker (having less loop area) on average than the top portion. From experimental tests, delta velocity had the best results on this panel, yet  $\tau$  resulted with a very

good total flaw detection as well.

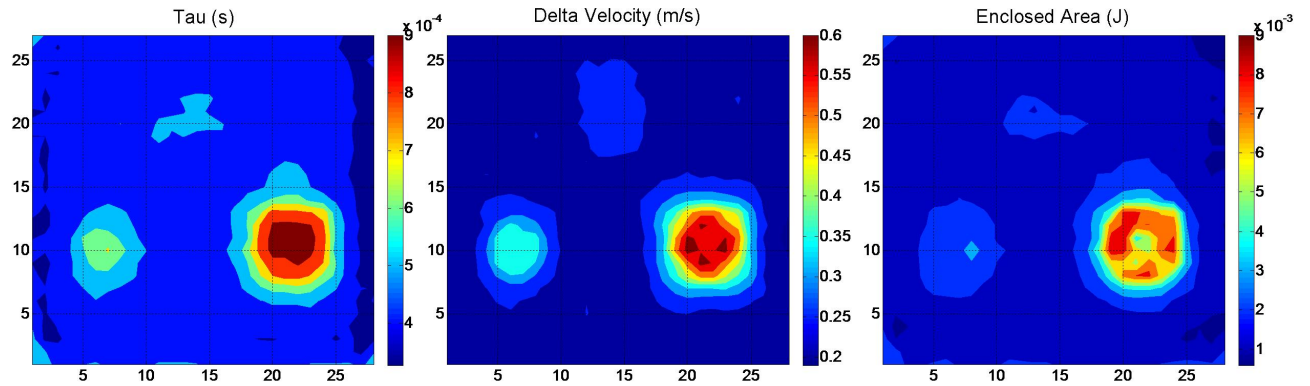


Figure 6.35 Contour images taken from Bell Helicopter panel C

Finally, the results of the third test panel are displayed in Fig. 6.35. This panel is composed of fiberglass face sheets with a honeycomb Nomex core. The core size is the smallest of the three panels. All three methods displayed very good results for this panel, each having very uniform baselines and very good flaw distinction. Although much information is unknown about these flaws, the sizes and shapes can be determined quite easily due to the clear images produced by all three methods. Even the severity of the flaws can be deduced from these images, which is often times not possible when using ultrasonic transduction.

### 6.3.6 FUTURE WORK

The acceleration integration method displayed very promising initial results, yet there is much work required to be completed in the future. A more reliable form of initial velocity selection must be developed. Setting displacement equal to zero at the point in time where the acceleration curve reaches a minimum, Minimum Acceleration Method, proved to work very well for the Bell Helicopter panels, yet intuitively, this method is not the most logical. It is assumed the accelerometer would register zero acceleration as it leaves the surface of the panel, not a negative acceleration. In order to acquire a full comprehension of this, the original

two methods for initial velocity calculation, Inflection Point Method and Zero Acceleration Method, should be studied further. A clearer understanding of the reason these methods do not work may shed some light upon either why the third method does work or provide a better method for initial velocity calculation. The fact that the accelerometer may leave the surface before the panel has returned to its original shape was not addressed in this research. A study of the impact history, including very accurate measurements of the motion of the transducer as well as the panel surface, may also help develop a more effective initial velocity selection technique.

A fast data acquisition method must also be developed. The current method for collecting the waveforms of the accelerometer made use of an oscilloscope and pre-amplifier. The process of collecting data over a 10 by 10 centimeter grid could take up to an hour, which is clearly unacceptable when considering the inspection of a real part. For use in the field, a simple and portable device is needed with which technicians can be easily trained. The study of hysteresis has many hurdles to overcome before it can make its way onto the hanger floor; however, the process shows promise and holds the possibility of becoming a robust nondestructive evaluation technique.

## CHAPTER 7. CONCLUSION

This thesis discussed many types of damages contained within honeycomb composite materials and a host of techniques used to detect them. Emphasis was given to the technique developed throughout the course of the research, which made use of the hysteresis effect in the stress-strain curve when loading a structure over a damaged region. This technique is an extension of the tap test and is showing much promise in the early stages of its development. The difference between static and dynamic loading was discussed as well as its importance when generating hysteresis loops. The change from static to dynamic was a large improvement, allowing the method to be several orders of magnitude faster than the original static loading technique and only requires one-sided access to the structure. There were many obstacles which needed to be overcome when switching from static to dynamic loading, which resulted in a slow development; yet a solid technique emerged. There is still much more research to be performed involving this method, where some uncertainties must be addressed.

Many established techniques were discussed, which were used to verify the technique developed. Air coupled ultrasonic transmission and the tap test were the two techniques mainly used to authenticate and perform baseline images for comparison with later experimental techniques. These two techniques were discussed in detail, although no real developments were made to these techniques during the course of the research; they were simply used as a reference.

When air coupled ultrasonic scanning was used on the honeycomb composites, the honeycomb structure would produce very distracting hexagonal patterns in the resulting image. A program for reducing these distracting patterns was developed throughout this research and outlined in this thesis. The two dimensional Fourier Transform is a very popular technique used in image processing. The written program utilized this technique specifically for filtering



out patterns in the ultrasonic C-Scans of honeycomb composites. Several features are contained within this program, which can be used to eliminate the patterns in the image caused by the double cell walls in the honeycomb composite.

In conclusion, the techniques developed showed very favorable results and displayed the ability to improve existing inspection techniques. Although it could seem like relatively small steps were taken toward the development of a usable NDE technique, it is a step none-the-less. Improvements on existing techniques will always be crucial; allowing us to step further, making our materials better, stronger, and safer.

## BIBLIOGRAPHY

- [1] Baker, A. Dutton, S. Kelly, D. (2004). Composite Materials for Aircraft Structures. *American Institute of Aeronautics and Astronautics, Inc.*
- [2] Shull, B.E. grey, J.N. (1989). X-Ray Measurement and Porosity In Graphite/Polyimide Composites. *Review of Progress In QUANTATATIVE NONDESTRUCTIVE EVALUATION Vol. 8B, pg. 1589*
- [3] Hsu, D. (2006). Nondestructive Evaluation of Damage in Composite Structures. *American Society for Composites Meeting*
- [4] Kommareddy, V. (2003). Air-coupled ultrasonic measurements in composites. *Iowa State University.*
- [5] National Instruments (2008). Fundamentals of Ultrasonic Imaging and Flaw Detection. <http://zone.ni.com/devzone/cda/tut/p/id/3368>  
*Date Referenced: 3/10/08*
- [6] Kang, K. Choi, M. Kim, K. Cha, Y. Kang, Y. Hong, D. Yang, S. (2006). Inspection of Impact Damage in Honeycomb Composite Plate By ESPI, Ultrasonic Testing, and Thermography. *Asia-Pacific Conference on NDT, 5th - 10th Nov. 2006*
- [7] Shepard, S.M. Ahmed, T. Lhota, J.R. (2004). Experimental Considerations in Vibrothermography. *SPIE Thermosense, April 12-16, 2004*
- [8] Rosencwaig, A. Opsal, J. (1986). Thermal Wave Imaging and Thermoacoustic Detection. *IEEE Transaction on Ultrasonics, Ferroelectrics, and frequency control, Vol. UFFC33, No.5*

- [9] Kalms, M. (2005). Mobile Shearography *The International Society of Optical Engineers April, 2005, Vol. 10, No. 4*
- [10] Hsu, D. Barnard, D. Peters, J. Dayal, V. (2000). Physical Basis of Tap Test as a Quantitative Imaging Tool for Composite Structures on Aircraft. *Review of Progress in Quantitative Nondestructive Evaluation*.
- [11] Zukas, J.A. Nicholas, T. Swift, H.F. Greszczuk, L.B. Curran, D.R. (1982). Damages in Composite Materials due to Low Velocity Impact. *Impact Dynamics. John Wiley and Sons, Inc. pp. 55-94*
- [12] Cawley, P. (1990). Low Frequency NDT Techniques for the Detection of Disbonds and Delaminations. *British Institute of Non-Destructive Testing, Vol.32, No.9, September 1990*
- [13] Findeis, D.M. Gryzagoridis, J. (2007). Low Frequency NDT Techniques for the Detection of Disbonds and Delaminations. *Mech. Eng. Dept, University of Cape Town, <http://www.ndt.uct.ac.za/Papers/ppv97.pdf> Date Referenced: 3/13/2008*
- [14] Steward, E.G. (1983). Fourier Optics an introduction. *Ellis Horwood Limited*
- [15] Brayer, J. (2007). Introduction to Fourier Transforms for Image Processing. *<http://www.cs.unm.edu/brayer/vision/fourier.html> Date Referenced: 1/29/08*
- [16] Promath4, developed by Teratech Inc., Rockville, MD 20850-5330 USA
- [17] Pavlidis, T. (2003). Algorithms for Graphics and Image Processing. *Computer Science Press*.
- [18] Roach, D. Rackow, K. (2003). Improving In-Service Inspection of Composite Structures: It's a Game of CATT and MAUS. *2003 NASA/FAA/DoD Aging Aircraft Conference*.
- [19] Maldague, X. (2007). Introduction to NDT by Active Infrared Thermography.

[20] Cripps, D. (2007). [www.Netcomposites.com](http://www.Netcomposites.com) - Guide to Composites.

<http://www.netcomposites.com/education.asp?sequence=2>

*Date Referenced: 1/29/08*

[21] Hoffman, F.M. (1997). An Introduction to Fourier Theory.

[http://lanoswww.epfl.ch/studinfo/courses/cours\\_dynsys/extras/Hoffman\(1997\)](http://lanoswww.epfl.ch/studinfo/courses/cours_dynsys/extras/Hoffman(1997))

[\\_An\\_Introduction\\_to\\_Fourier\\_Theory.pdf](#)

*Date Referenced: 1/29/08*